

MASSIVE YOUNG STELLAR OBJECTS IN THE GALACTIC CENTER. I. SPECTROSCOPIC IDENTIFICATION FROM *SPITZER*/IRS OBSERVATIONS

DEOKKEUN AN¹, SOLANGE V. RAMÍREZ², KRIS SELLGREN³, RICHARD G. ARENDT⁴, A. C. ADWIN BOOGERT²,
THOMAS P. ROBITAILLE^{5,6}, MATHIAS SCHULTHEIS⁷, ANGELA S. COTERA⁸,
HOWARD A. SMITH⁵, SUSAN R. STOLOGY⁹

Accepted for the publication in ApJ

ABSTRACT

We present results from our spectroscopic study, using the Infrared Spectrograph (IRS) onboard the *Spitzer Space Telescope*, designed to identify massive young stellar objects (YSOs) in the Galactic Center (GC). Our sample of 107 YSO candidates was selected based on IRAC colors from the high spatial resolution, high sensitivity *Spitzer*/IRAC images in the Central Molecular Zone (CMZ), which spans the central ~ 300 pc region of the Milky Way Galaxy. We obtained IRS spectra over $5 \mu\text{m}$ to $35 \mu\text{m}$ using both high- and low-resolution IRS modules. We spectroscopically identify massive YSOs by the presence of a $15.4 \mu\text{m}$ shoulder on the absorption profile of $15 \mu\text{m}$ CO₂ ice, suggestive of CO₂ ice mixed with CH₃OH ice on grains. This $15.4 \mu\text{m}$ shoulder is clearly observed in 16 sources and possibly observed in an additional 19 sources. We show that 9 massive YSOs also reveal molecular gas-phase absorption from CO₂, C₂H₂, and/or HCN, which traces warm and dense gas in YSOs. Our results provide the first spectroscopic census of the massive YSO population in the GC. We fit YSO models to the observed spectral energy distributions and find YSO masses of $8\text{--}23 M_{\odot}$, which generally agree with the masses derived from observed radio continuum emission. We find that about 50% of photometrically identified YSOs are confirmed with our spectroscopic study. This implies a preliminary star formation rate of $\sim 0.07 M_{\odot} \text{ yr}^{-1}$ at the GC.

Subject headings: infrared: ISM — ISM: molecules — stars: formation — Galaxy: nucleus

1. INTRODUCTION

Our Galactic center (GC), at a distance of 7.9 ± 0.8 kpc (Reid et al. 2009), is the closest galactic nucleus, observable at spatial resolutions unapproachable in other galaxies ($1 \text{ pc} \approx 26''$). The extent of the GC region is defined by a region of relatively high density molecular gas ($n_{\text{H}_2} \sim 10^4 \text{ cm}^{-3}$; Bally et al. 1987), covering the inner $200 \text{ pc} \times 50 \text{ pc}$ ($170' \times 40'$), called the Central Molecular Zone (CMZ). The CMZ produces 5%–10% of the Galaxy's infrared and Lyman continuum luminosity and contains 10% of its molecular gas (Smith et al. 1978; Nishimura et al. 1980; Bally et al. 1987, 1988; Morris & Serabyn 1996). The CMZ exhibits extreme conditions with high gas temperature, pressure, turbulence, strong magnetic field strengths and strong tidal shear (Serabyn & Morris 1996; Fatuzzo & Melia 2009). As a result, star formation in the CMZ may be altered or suppressed.

The CMZ, nevertheless, shows several signposts of recent massive star formation, such as (compact) H II regions and supernova remnants. In addition, there are massive young stars (ages of $\sim 2\text{--}7$ Myrs; Krabbe et al. 1991; Figer et al. 1999)

in three known discrete star clusters – the Central, Quintuplet, and Arches clusters – which make the CMZ distinctly different from the Galactic bulge with its predominantly old stellar population (Frogel & Whitford 1987). Nevertheless, it has been unclear how star formation proceeds in this hostile environment. There have been several studies in the literature that identified young stellar object (YSO) candidates in the GC based on infrared photometry (e.g., Felli et al. 2002; Schuller et al. 2006; Yusef-Zadeh et al. 2009). The high and patchy extinction towards the GC ($A_V \approx 30$) and its mix of young and old stellar populations, however, mean that spectroscopic observations are required to confirm YSO identifications. This is because red giants and asymptotic giant branch (AGB) stars (also part of the GC stellar population) can look like YSOs from broad-band photometry, if they are heavily dust attenuated (e.g., Schultheis et al. 2003).

The GC provides a unique opportunity to investigate circumnuclear star formation with an unprecedented spatial resolution. We announced the first spectroscopic identification of massive YSOs in the CMZ (An et al. 2009, hereafter A09), using the Infrared Spectrograph (IRS; Houck et al. 2004) onboard the *Spitzer Space Telescope* (Werner et al. 2004). In this paper, we follow up our initial exploration of the IRS data set in A09 and refine our methods to identify YSOs in the CMZ, aiming at providing a list of spectroscopically confirmed YSOs as tracers of the early stages of star formation in the GC. As described and employed in A09, our selection criteria for YSOs are based on gas- and solid-phase absorption from mid-IR spectroscopy. This includes solid-phase absorption from the CO₂ bending mode (e.g., Gerakines et al. 1999) and gas-phase absorption from C₂H₂, HCN, and CO₂ (e.g., Lahuis & van Dishoeck 2000; Boonman et al. 2003; Knez et al. 2009). We look for signatures of CO₂ ice mixed with a large amount of CH₃OH

¹ Department of Science Education, Ewha Womans University, Seoul 120-750, Korea; deokkeun@ewha.ac.kr.

² NASA Exoplanet Science Institute, California Institute of Technology, Mail Stop 100-22, Pasadena, CA 91125.

³ Department of Astronomy, The Ohio State University, 140 West 18th Avenue, Columbus, OH 43210.

⁴ CRESST/UMBC/GSFC, Code 665, NASA/Goddard Space Flight Center, 8800 Greenbelt Road, Greenbelt, MD 20771.

⁵ Harvard-Smithsonian Center for Astrophysics, 60 Garden Street, Cambridge, MA 02138.

⁶ Spitzer Postdoctoral Fellow.

⁷ Observatoire de Besançon, 41bis, avenue de l'Observatoire, 25000 Besançon, France.

⁸ SETI Institute, 515 North Whisman Road, Mountain View, CA 94043.

⁹ Spitzer Science Center, California Institute of Technology, Mail Code 220-6, 1200 East California Boulevard, Pasadena, CA 91125.

ice. This combination has been observed towards high-mass YSOs and low-mass YSOs (Gerakines et al. 1999; Pontoppidan et al. 2008; Zasowski et al. 2009; Seale et al. 2011), but not toward field stars behind molecular clouds (Gerakines et al. 1999; Bergin et al. 2005; Knez et al. 2005; Whittet et al. 2007, 2009).

In § 2 we summarize the IRS target selection criteria and data reduction. In § 3 we describe our spectroscopic identification of YSOs, showing that 15%–30% of our 107 targets are massive YSOs. We measure the extinction for YSOs and possible YSOs, along with column densities of solid-phase and gas-phase molecular absorbers. In § 4 we examine properties of these YSOs and possible YSOs, and derive a preliminary estimate of the star formation rate in the GC.

2. METHODS

In this section we describe procedures for the sample selection, spectroscopic follow-up observations, and IRS data reduction. Parallel information on these subjects can be found in A09, but here we repeat this for the reader’s convenience with additional details where there has been improvements in the data reduction steps.

2.1. *Spitzer*/IRS Sample

Our 107 spectroscopic targets (Table 2) were selected from the GC point source catalog (Ramírez et al. 2008) extracted from the IRAC images of the CMZ (Stolovy et al. 2006) made using the Infrared Array Camera (IRAC; Fazio et al. 2004) onboard the *Spitzer Space Telescope*. These images cover $280 \text{ pc} \times 200 \text{ pc}$ in the four IRAC channels ($3.6 \mu\text{m}$, $4.5 \mu\text{m}$, $5.8 \mu\text{m}$, and $8.0 \mu\text{m}$) with uniform high sensitivity. Compared to earlier imaging surveys of this region, such as that from the *Midcourse Space Experiment* (MSX; Price et al. 2001) or ISOGAL (Omont et al. 2003), the IRAC images have a higher spatial resolution ($\approx 2''$ vs. $> 6''$ of earlier surveys), which has led not only to a better estimate of source fluxes, but also to more accurate source positions for follow-up spectroscopic observations.

The spectroscopic sample was selected using IRAC color criteria based on the Whitney et al. (2004) study of the giant H II region RCW 49. Whitney et al. determined the locations of YSOs with $2.5 M_{\odot}$, $3.8 M_{\odot}$, and $5.9 M_{\odot}$ on the IRAC color-magnitude diagrams, using radiative transfer models described in Whitney et al. (2003). From this we chose an initial color criterion ($[3.6] - [8.0] \geq 2.0$; Whitney et al. 2004). We added a latitudinal constraint ($|b| < 15'$) to increase the probability that the objects are located at the distance of the GC (8 kpc; Reid et al. 2009) rather than in one of the several intervening spiral arms along the line of sight. We note that the range of this latitude selection is about 5 times larger than the scale height of photometric YSO candidates ($\sim 7 \text{ pc}$) in Yusef-Zadeh et al. (2009). These color and position constraints provided an initial sample of 1207 objects from the GC point source catalog.

We combined the IRAC photometry with Two Micron All Sky Survey (2MASS) photometry (JHK_s ; Skrutskie et al. 2006) and ISOGAL $7 \mu\text{m}$ and $15 \mu\text{m}$ point-source catalogs. Note that $24 \mu\text{m}$ Multiband Imaging Photometer for *Spitzer* (MIPS) observations at the GC were not available at the time when our IRS sample was chosen. Among the initially selected 1207 objects, 336 had photometry in at least 5 bandpasses, which allowed reliable spectral energy distribution (SED) fitting. We used the SED fitting tool developed by Robitaille et al. (2007), which makes use of a grid

of 200,000 YSO models (Robitaille et al. 2006) to estimate YSO parameters, such as the mass of a central object (see § 4.1). For those objects with photometry in fewer than five bandpasses, we instead applied color constraints based on the work of Whitney et al. (2004) of $[3.6] - [4.5] \geq 0.5$, $[4.5] - [5.8] \geq 0.5$, and $[5.8] - [8.0] \geq 1.0$.

The SED fitting and additional IRAC color constraints narrowed our sample down to about 200 objects, which were then further inspected using IRAC three-color images. The sources were evaluated by their distinctiveness (i.e., whether sources are easily distinguishable from the background) and their local background emission. Among 200 objects examined, 112 were found to exhibit the necessary distinctiveness within the IRS slit widths.

A literature search was performed on the 112 objects, yielding matches to 43 previously studied sources: 25 sources were previously-identified photometric YSO candidates, 4 were OH/IR stars, one was a Wolf-Rayet star, and the remaining 13 sources were others (e.g., radio sources, X-ray sources, etc). Note that nearly 60% ($\approx 25/43$) of the objects had been selected as YSO candidates by other methods. The 4 OH/IR stars and the Wolf-Rayet star were discarded from the final sample, giving a total of 107 massive YSO candidates. The spatial location of the 107 massive YSO candidates of our sample is shown in Figure 1.

In spite of our efforts to exclude OH/IR stars from our YSO sample, we later realized that several of our targets appear to be coincident with a stellar maser source and/or a long-period variable (SSTGC 284291, 425399, 564417, 619964, 660708, 696367, and 711462). SSTGC 517724 is now identified as an OB supergiant by Mauerhan et al. (2010). These sources known not to be YSOs have been helpful in refining our spectroscopic YSO selection criteria.

Massive YSOs are our primary targets for the follow-up spectroscopic observations (§ 2.2) because our adopted color selection criteria set the lower limit on the mass of the central object to be $M_* \gtrsim 2.5 M_{\odot}$ (Whitney et al. 2003, 2004). In addition, the source confusion limit in the input GC point source catalog (see Figure 12 in Ramírez et al. 2008), together with the 8 kpc distance to the GC (Reid et al. 2009) and $A_V \sim 30 \text{ mag}$ of visual extinction, limits us to detecting YSOs with masses $\gtrsim 6 M_{\odot}$ (see § 4). Thus any YSO we identify in this paper is a *massive* YSO.

2.2. Observations

Our IRS observations with a total integration time of 56 hours were carried out in May and October 2008 (see Table 2) as part of *Spitzer* Cycle 4 (Program ID: 40230, PI: S. Ramírez). We observed our 107 targets with both high- and low-resolution IRS modules: short-high (SH; $9.9 \mu\text{m}$ – $19.6 \mu\text{m}$, $\lambda/\Delta\lambda \sim 600$), long-high (LH; $18.7 \mu\text{m}$ – $37.2 \mu\text{m}$, $\lambda/\Delta\lambda \sim 600$), short-low (SL; $5.2 \mu\text{m}$ – $14.5 \mu\text{m}$, $\lambda/\Delta\lambda \sim 60$ – 127), and long-low (LL; $14 \mu\text{m}$ – $38 \mu\text{m}$, $\lambda/\Delta\lambda \sim 57$ – 126).

In Table 3 we list IRS modules used in the current analysis for each of the sources that are spectroscopically identified as a YSO or possible YSO in this paper (see § 3.1). Most of these targets were observed with all of the four IRS modules. We did not obtain spectra with the SL module for some of the 107 YSO candidates, including possible YSO SSTGC 610642, because of saturation in the IRS peak-up arrays (see below). For a few sources we rejected data in the first order of LL (LL1; $19.5 \mu\text{m}$ - $38.0 \mu\text{m}$) because a large fraction of pixel values were flagged as invalid.

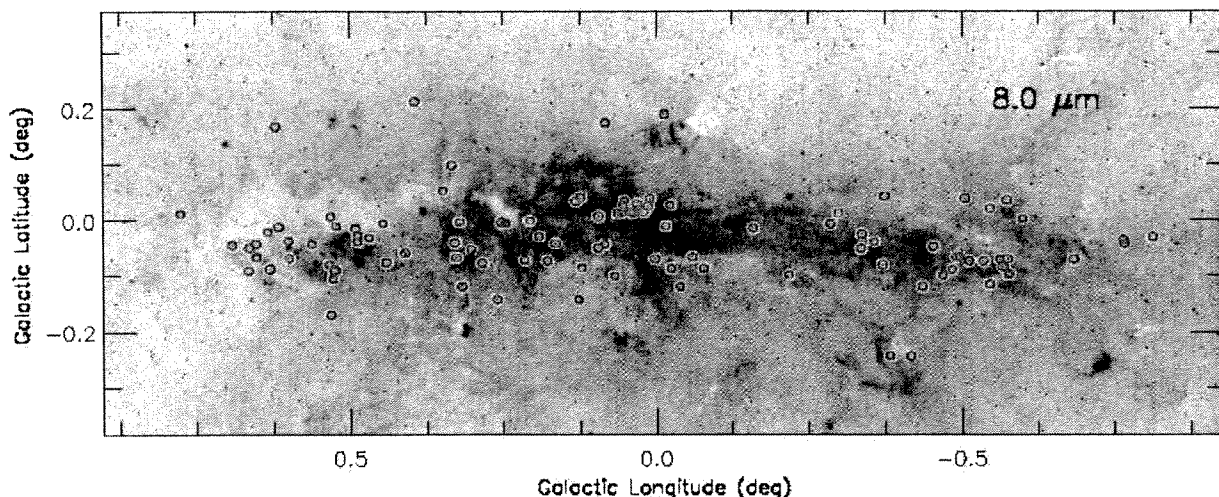


FIG. 1.— Spatial distribution of 107 IRS targets on the IRAC $8.0 \mu\text{m}$ image (Stolovy et al. 2006). The image shows the entire CMZ covering approximately $100' \times 40'$ centered on the GC. Our IRS targets (shown in circles) were selected from the point sources of this survey and they are uniformly distributed over the CMZ.

We divided our sample into four subsamples according to their IRAC [8.0] magnitudes: $[8.0] \leq 6 \text{ mag}$ ($N = 30$ objects), $6 \text{ mag} < [8.0] \leq 7 \text{ mag}$ ($N = 28$), $7 \text{ mag} < [8.0] \leq 8 \text{ mag}$ ($N = 28$), and $[8.0] > 8 \text{ mag}$ ($N = 21$). Exposure times were determined for each brightness subsample to achieve a signal-to-noise (S/N) ratio of at least 50 in SH and SL, and a minimum S/N of 10 in LH and LL. Our exposure times are 6 sec–120 sec in SH, 6 sec–60 sec in LH, 6 sec–14 sec in SL, and 6 sec in LL modules. Subsamples were further grouped based on spatial location. These groupings allowed us to observe 107 sources using nine “fixed cluster” target observations, a strategy which proved to greatly increase the observing efficiency by reducing overheads due to telescope movement. Each object was observed in the IRS staring mode with 4 exposures per source (2 cycles) to properly correct for bad pixels.

Our observations were carried out without specific IRS peak-up sequences, since target coordinates were accurate enough ($< 1''$; Ramírez et al. 2008) for our science goals. In addition, the background at the GC is too high for a peak-up sequence to work even using a 2MASS source. In fact, the background at the GC is so high that constraints were placed on the observing dates (which determine the telescope roll angle) to avoid saturation of the IRS peak-up arrays. Such saturation leads to incorrect droop corrections in the standard IRS pipelines and causes various defects on SL frames (where the peak-up arrays are located). The SL observations were not carried out for 21 out of 107 targets because of saturation in the peak-up arrays regardless of the date of observation.

Multiple off-source measurements at several different locations were carried out to derive background spectra around each target, because strong and spatially variable background at the GC can affect resulting line and/or continuum emission from the source. Since the high-resolution slits are not long enough to take both source and background measurements simultaneously, we located four background positions around each target ($\sim \pm 1'$ offsets in right ascension, $\sim \pm 1'$ offsets in declination). Specific background positions for both SH and LH were determined to avoid background sources and to properly interpolate background emission near the source position over a $\sim 1'$ scale. The longer slit sizes of the low-

resolution modules permit background measurements along the on-source slit; we also identified two additional background positions that are $\sim \pm 1'$ away in the direction perpendicular to the SL or LL slit. These dedicated background slits for SL and LL were centered on two of the high-resolution background positions.

Figure 2 displays the IRS slit positions for on-source (*left*) and off-source (*right*) measurements for one of our sources (SSTGC 797384). Source and background spectra were taken consecutively to minimize zodiacal light and instrumental variations. Each order of SL or LL was used to observe a target, and different orders cover different parts of the sky near each target. The low ecliptic latitude of the GC restricts the LL slits to a position angle (PA) of $\sim \pm 90^\circ$ and the SL slits to a PA of $\sim 0^\circ$ or 180° .

2.3. Data Reduction

We began reducing the high-resolution IRS spectra from the basic calibrated data (BCD), while we started with coadded products (post-BCD) for the low-resolution spectra. We used the S18.7 version of the IRS pipeline for both. On the LH frames we applied the DARKSETTLE¹⁰ software package to correct for non-uniform dark currents. We corrected for rogue pixel values using the SSC software package IRSCLEAN¹. We only applied campaign rogue masks (Campaigns 50 and 55 for the spring and autumn runs, respectively), except in SL, where we applied our own edited version to mask out hot pixels at $\sim 10 \mu\text{m}$ in addition to campaign rogue pixels. We then used SPICE¹ to extract target and background spectra, and further corrected high-resolution spectra (SH, LH) for fringe patterns using the IRSFRINGE¹ package.

Four background spectra per target were extracted for the high-resolution (SH and LH) observations as four off-source pointings were obtained per target. For the low-resolution (SL and LL) observations, two background spectra were extracted from observations at the same positions as the high-resolution background observations and two background spectra were extracted along the on-source slit observations. For some ob-

¹⁰ The SSC software packages can be found at <http://ssc.spitzer.caltech.edu/dataanalysisistools/tools/>.

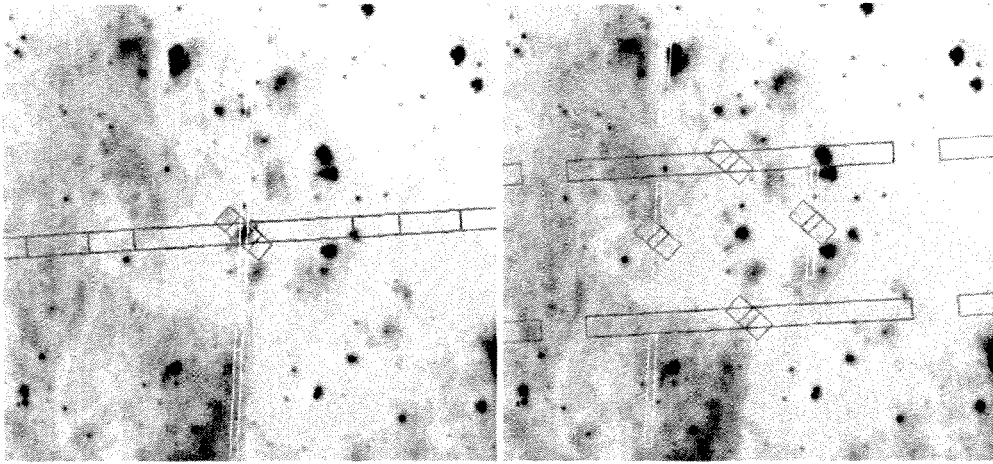


FIG. 2.— IRAC 8.0 μm image showing a $4' \times 4'$ field of view, centered on one of our IRS targets (SSTGC 797384). *Left*: positions of all IRS slits (SL: red, LL: yellow, SH: magenta, and LH: green) for on-source measurements. *Right*: Off-source measurements, showing background positions around the source. Similar slit formations were adopted for all of the spectroscopic targets. The four off-source pointings were observed to derive a background spectrum for each source, because of strong and spatially variable background towards the GC.

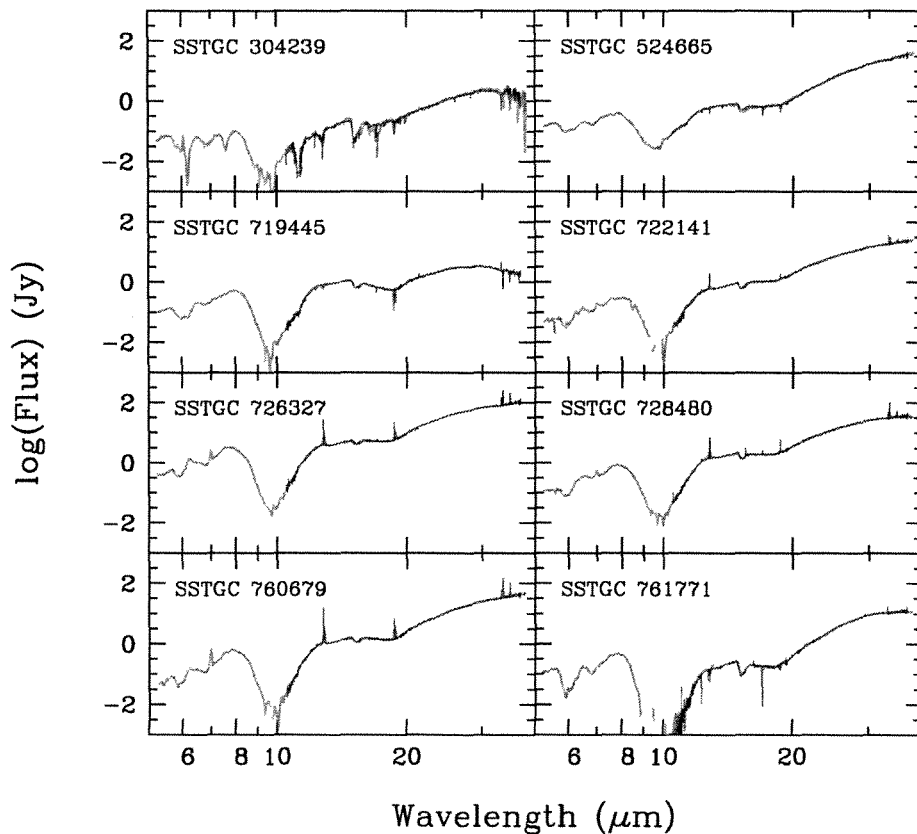


FIG. 3.— IRS spectra of spectroscopically identified YSOs. Orange lines are low-resolution (SL, LL modules) spectra, and green lines are high-resolution (SH, LH modules) spectra. The high-resolution spectra were scaled to match the flux in low-resolution modules (see text).

jects, the high-resolution background slits were not coincident with the on-source low-resolution slits. For these, we inspected the slit positions on an IRAC/MIPS composite image to determine the extraction position along the on-source SL or LL slit that was closest in flux and position to the high-resolution background slits.

For each module and for each target, we were able to extract four background spectra, that we used to estimate the target background by making a linear interpolation of the back-

ground flux at the source position at each wavelength. Our interpolation scheme estimates the background flux gradient over a $\sim 1'$ angular scale, since each background pointing is $\sim 1'$ away from the science target. If the background emission is varying over a smaller angular scale, then background subtraction would be more uncertain.

We found that spectra extracted from various IRS modules usually do not match with each other at overlapping wavelengths, primarily due to the different sizes of the slit en-

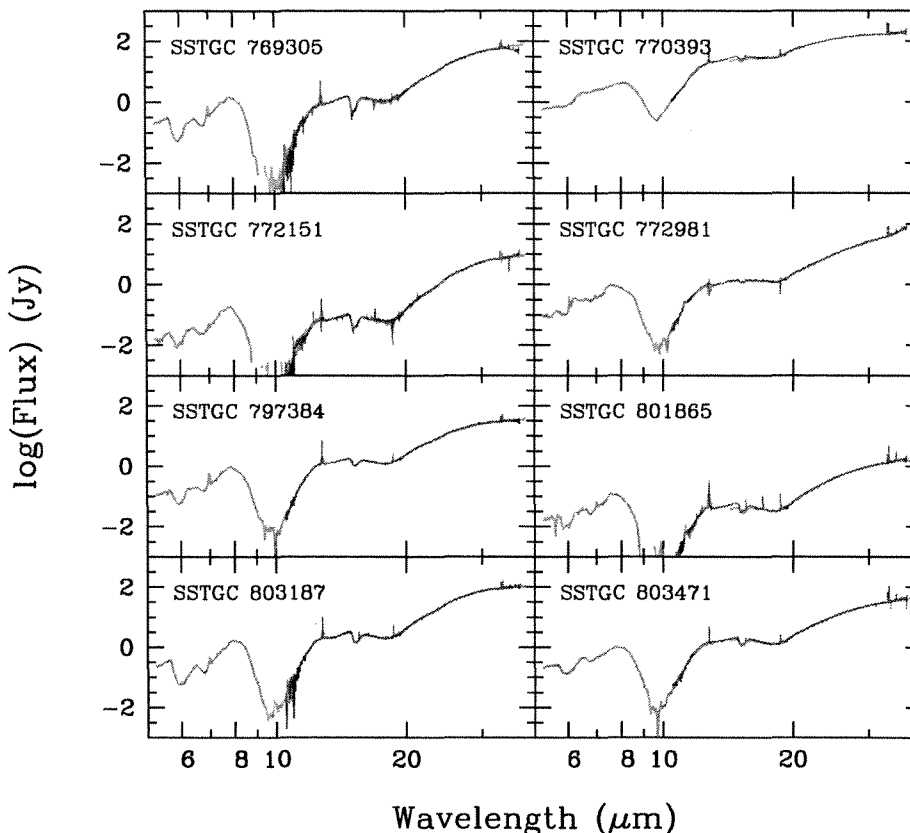


FIG. 4.— Cont'd. Same as in Figure 3.

trances. The SL and LL modules have $3.7''$ and $10.7''$ slit widths, respectively, while the slit entrances of SH and LH modules are $4.7'' \times 11.3''$ and $11.1'' \times 22.3''$, respectively. Therefore, contamination by point sources and/or extended emission at the GC can easily lead to a flux mismatch among the various IRS modules.

To obtain internally consistent fluxes from all of the IRS modules, we scaled the spectra to match the fluxes from the second order of LL (LL2; $14 \mu\text{m} - 21 \mu\text{m}$). On the longer wavelength side, we scaled the LL1 spectrum to the LL2 spectrum by estimating a median flux ratio for the two modules in the overlapping wavelength region. We masked known emission features and rejected points that were more than 3σ away from the median flux ratio. On the shorter wavelength side, the scaling was done in a step-by-step fashion. We first scaled the SH spectrum to the base flux of the LL2 spectrum (before correcting for order tilts; see below). We then matched the spectrum in the first order of SL (SL1; $7.4 \mu\text{m} - 14.5 \mu\text{m}$) to the SH spectrum, then scaled the flux in SL3 (bonus order; $7.3 \mu\text{m} - 8.7 \mu\text{m}$) to the SL1 spectrum, and finally scaled the flux in the second order of SL (SL2; $5.2 \mu\text{m} - 7.7 \mu\text{m}$) to SL3. We can describe this concisely as LL2 \rightarrow LL1, and LL2 \rightarrow SH \rightarrow SL1 \rightarrow SL3 \rightarrow SL2. If a source was not clearly separated from extended background emission in LL2, we opted to choose the SL1 spectrum as the base flux for scaling. In this case, the flux calibration was done in the following sequences: SL1 \rightarrow SH \rightarrow LL2 \rightarrow LL1, and SL1 \rightarrow SL3 \rightarrow SL2.

Scaling factors applied to each module are shown in Table 3. The second column in Table 3 shows which mod-

ule was used as the baseline for the flux calibration for each target. Either large or small scaling factors are found in LL for SSTGC 360559, SL for SSTGC 773985, and LL for SSTGC 801865. These objects are faint ($[8.0] = 7.6$ mag and 8.8 mag for SSTGC 360559 and 801865, respectively, while SSTGC 773985 was not detected in this bandpass) on top of bright or saturated background emission on MIPS [24] images. As a result, their mid-IR fluxes are heavily contaminated by background emissions at $\lambda \gtrsim 20 \mu\text{m}$, leading to an over-estimation of flux from the target slit.

Order-tilt features remained in about 30 high-resolution spectra, after applying IRSFRINGE to SH and LH and DARKSETTLE to LH. To remove this artifact, we applied a 1st order polynomial to each high-resolution spectral order to force it to match the re-scaled low-resolution spectra. In addition, three sources showed scalloping features in their high-resolution spectra; a 2nd order polynomial was applied to correct for this artifact. Individual spectra from various orders were then merged together using a linear ramp.

Some data were excluded from the analysis due to problems in a particular spectrum, such as saturation, excess bad pixels, or a poor match in background level. The last column in Table 3 lists any excluded data. Each target was observed at two different nod positions in each module; any nod positions that were excluded for a particular module are also given in the last column of Table 3. A cardinal point (NSEW) given in parentheses in this column indicates that the background spectrum offset in that direction from the source was not included in the background determination for that module.

Figures 3–7 display spectra resulting from the above proce-

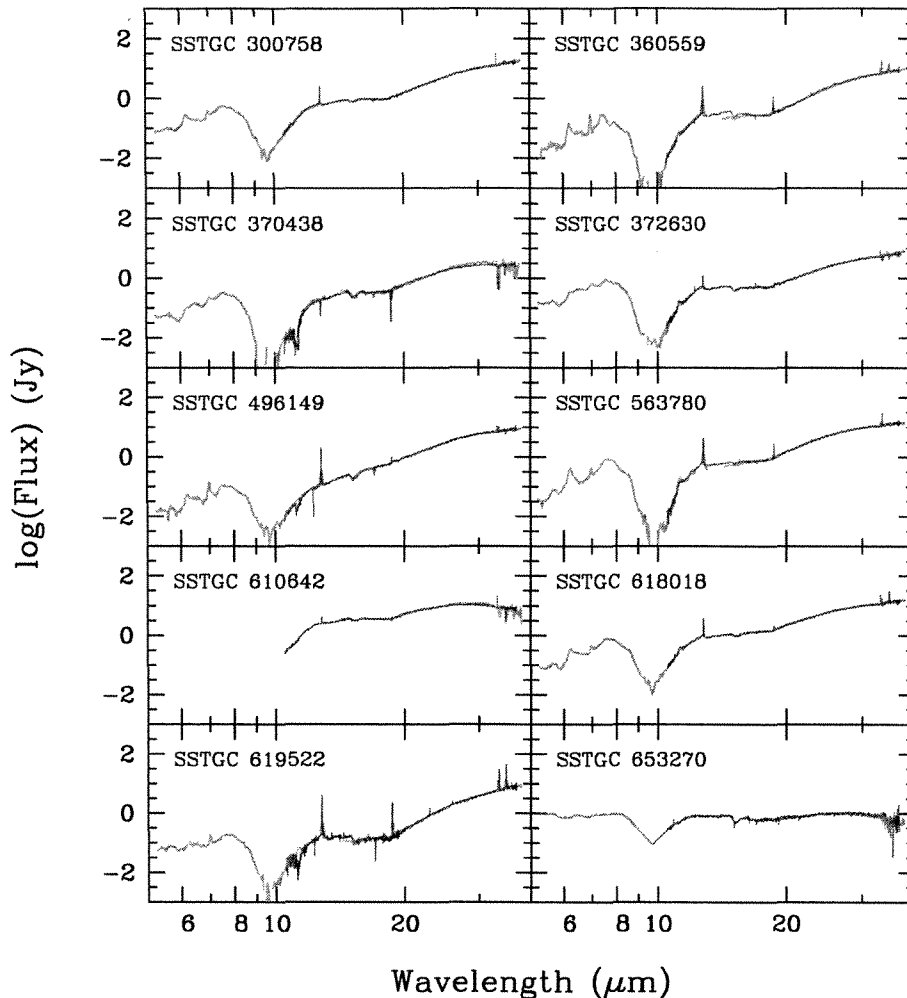


FIG. 5.— IRS spectra of possible YSOs. Line colors are the same as in Figure 3.

dures; orange lines are low-resolution spectra, and green lines represent high-resolution spectra. Only sources we spectroscopically identify as a YSO or possible YSO are shown in Figures 3–6. Spectra of known OH/IR, long-period variable, or OB supergiant stars in our sample are shown in Figure 7 for comparison.

There are several sources of flux uncertainty in our spectra: statistical, calibration (difference between different nods), and the varying background (this last is usually largest). This can cause spectral features observed in emission in the background appear in absorption in some spectra, such as the $11.3 \mu\text{m}$ polycyclic aromatic hydrocarbon (PAH) feature (e.g. SSTGC 304239), H_2 emission at $17.0 \mu\text{m}$ (e.g. SSTGC 761771), or forbidden lines such as $12.8 \mu\text{m}$ [Ne II] or $18.7 \mu\text{m}$ [S III] (e.g. SSTGC 670953). We have estimated the uncertainty due to background subtraction by comparing results derived by excluding one of the four background pointings from the interpolated background spectrum. Throughout our analysis, we have added these uncertainties in quadrature to derive final uncertainties in measured quantities such as the CO_2 ice column density.

3. RESULTS

3.1. Spectroscopic Identification of Massive YSOs in the GC

To study the $15 \mu\text{m}$ CO_2 ice absorption profile, we fitted five laboratory spectral components to the feature in all our 107 targets, following the same procedure described in A09. Figures 8–10 show the CO_2 ice decomposition for our YSOs, possible YSOs, and known stars for comparison, respectively. We describe below how we selected YSOs and possible YSOs based on this procedure.

First, we set a local continuum over $14.3 \mu\text{m} \leq \lambda \leq 16.5 \mu\text{m}$ using a 3^{rd} order polynomial to derive the optical depth. Then we used the modeling technique and laboratory data in Pontoppidan et al. (2008) to decompose the absorption profile with five laboratory spectral components; these are polar CO_2 ($\text{CO}_2:\text{H}_2\text{O} = 14 : 100$ at 10 K; dotted line, centered at $\sim 15.3 \mu\text{m}$), apolar CO_2 ($\text{CO}:\text{CO}_2 = 100 : 70$ at 10 K; dotted line, centered at $\sim 15.1 \mu\text{m}$), pure CO_2 (15 K; blue shaded), diluted CO_2 ($\text{CO}:\text{CO}_2 = 100 : 4$ at 10 K; black solid line), and $15.4 \mu\text{m}$ shoulder CO_2 (modeled with two Gaussians in wavenumber space; orange shaded). We found a best-fitting set of models from the non-linear least squares fitting routine MPFIT (Markwardt 2009).

Fitting results are shown in Table 4. The CO_2 ice column densities were estimated from the integrated absorption, adopting the integrated line strength $A = 1.1 \times 10^{-17} \text{ cm molecule}^{-1}$ (Gerakines et al. 1995). Background uncertainties were estimated by creating spectra with one of four

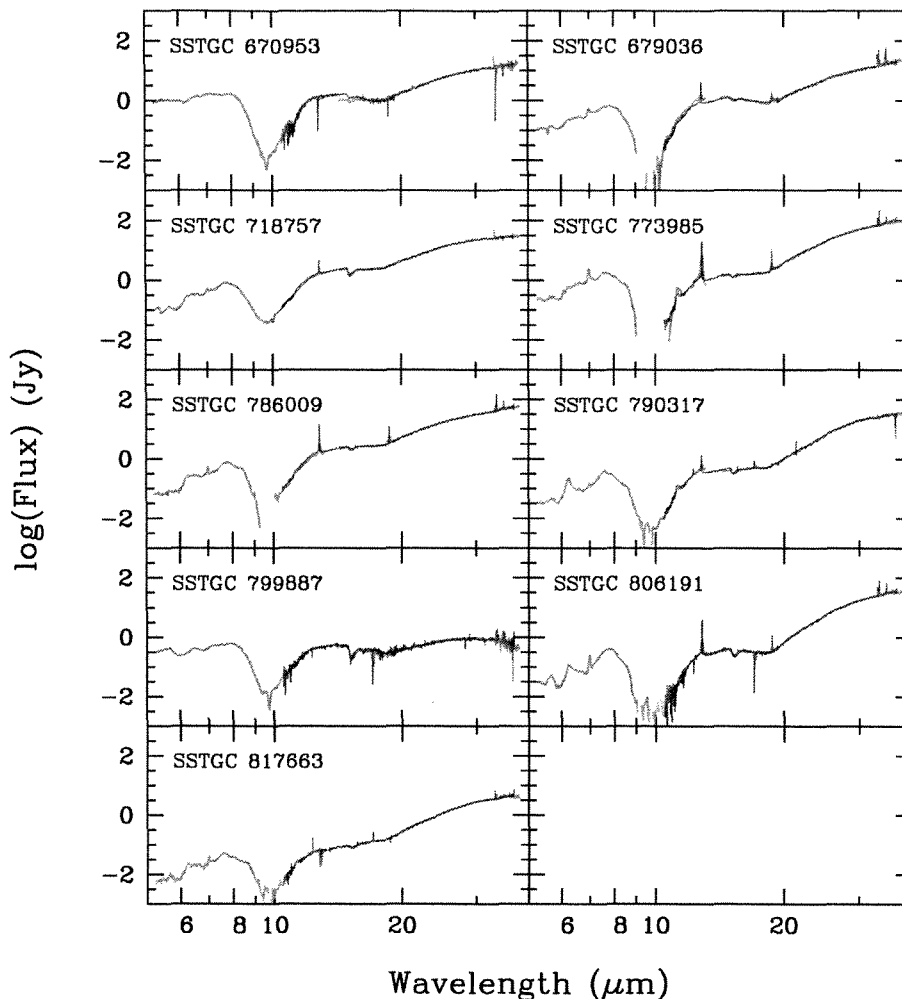


FIG. 6. — Cont'd. Same as in Figure 5.

background positions excluded from the interpolated background spectrum (§2) and then comparing the column densities derived from these spectra. We added these uncertainties in quadrature to the uncertainties from comparing column densities from spectra at the two nod positions, and to uncertainties in column densities due to the statistical uncertainties. The χ^2_{tot} and N_{tot} in Table 4 represent the total chi-square of the fit and the number of data points used in this fit. The goodness of fit is generally poor, implying either underestimated flux errors or our lack of knowledge of individual CO_2 ice models. Nevertheless, the ice decomposition still provides useful information on the nature of YSOs, as shown below. For comparison, fitting results for some known stellar sources are included in Table 4.

Our primary method of identifying YSOs from our IRS observations is the CO_2 ice absorption profile at $15 \mu\text{m}$, which is observed to have a different spectral shape in and around YSOs (Ehrenfreund et al. 1999; Dartois et al. 1999a). High-spectral resolution observations of many massive YSOs in our Galaxy (Gerakines et al. 1999) and in the Large Magellanic Cloud (Seale et al. 2011) found a “shoulder” at $15.4 \mu\text{m}$ on the CO_2 ice absorption profile. This $15.4 \mu\text{m}$ shoulder is thought to be due to the presence of CH_3OH -rich CO_2 ice grains (Ehrenfreund et al. 1999; Dartois et al. 1999a). Detailed fitting of the $15 \mu\text{m}$ CO_2 ice profile shows

that the $15.4 \mu\text{m}$ shoulder is weaker in low-mass protostars (Pontoppidan et al. 2008; Zasowski et al. 2009) and is not detected towards field stars behind several molecular clouds (Gerakines et al. 1999; Bergin et al. 2005; Knez et al. 2005; Whittet et al. 2007, 2009). Analysis of the $15 \mu\text{m}$ CO_2 ice profile along the lines of sight to the Central Cluster and to two dusty WC9 stars in the Quintuplet Cluster demonstrates that none of these three GC spectra shows a $15.4 \mu\text{m}$ shoulder on the $15 \mu\text{m}$ CO_2 ice absorption profile (Gerakines et al. 1999). Thus, the presence or absence of the $15.4 \mu\text{m}$ shoulder is an empirical – and quantitative – way in the GC of distinguishing YSOs from AGB stars behind molecular clouds.

The $15 \mu\text{m}$ CO_2 ice absorption profiles displayed in Figures 8–9 for 35 of our YSOs or possible YSOs (see below) show two absorption peaks, at $15.15 \mu\text{m}$ and $15.4 \mu\text{m}$. Many previously studied YSOs show a double-peaked absorption profile, but with peaks at shorter wavelengths of $15.10 \mu\text{m}$ and $15.25 \mu\text{m}$ (e.g., Gerakines et al. 1999; Pontoppidan et al. 2008; Seale et al. 2011). Double-peaked absorption at $15.10 \mu\text{m}$ and $15.25 \mu\text{m}$ is ascribed to pure CO_2 ices resulting from the crystallization of heated H_2O -rich ices (e.g., Gerakines et al. 1999; Pontoppidan et al. 2008). By contrast, Ehrenfreund et al. (1999) and Dartois et al. (1999a) interpret CO_2 ice absorption peaking at $15.15 \mu\text{m}$ as due to CO -rich CO_2 ices and absorption peaking at $15.4 \mu\text{m}$ as arising in

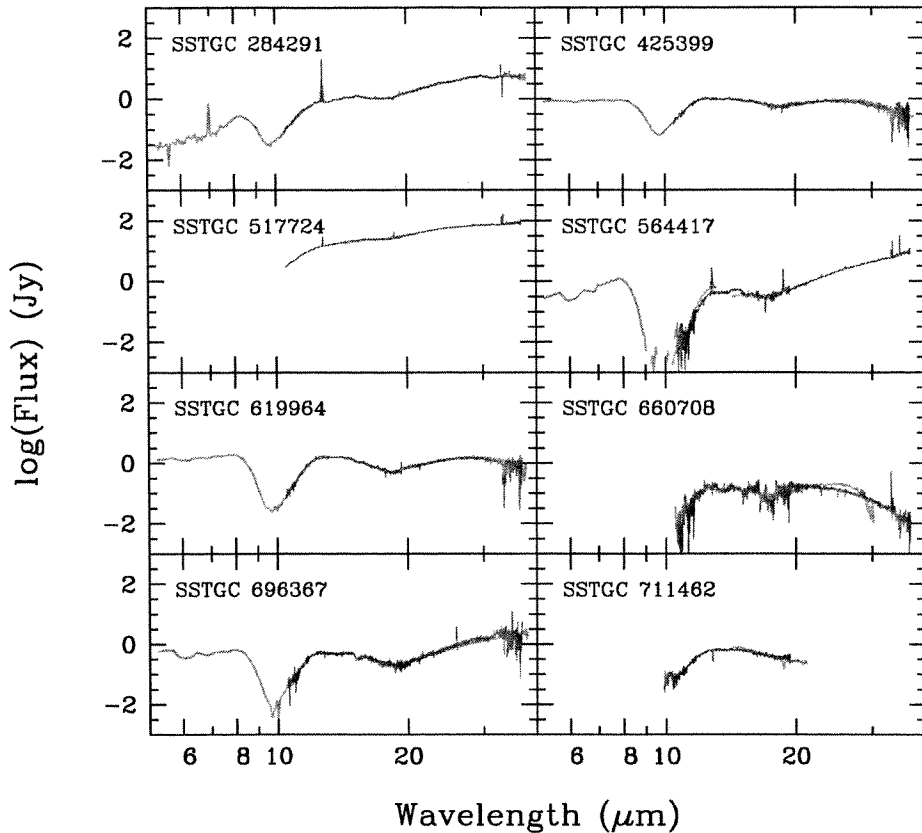


FIG. 7.— IRS spectra of known stars (non-YSOs) in our target sample. SSTGC 517724 is an OB supergiant star (Mauerhan et al. 2010) and the other targets are OH/IR stars or long period variables. Line colors are the same as in Figure 3.

CH₃OH-rich CO₂ ices.

We selected YSOs by requiring that the model fit to the observed 15 μm CO₂ ice profile significantly improves when the 15.4 μm shoulder is included in the model. We calculated the reduced χ^2 for fitting a four-component model (excluding the 15.4 μm shoulder) to the 15 μm CO₂ profile, as shown in the bottom panels in Figures 8–9. We then calculated the reduced χ^2 for fitting the five-component model (including the 15.4 μm shoulder). Finally, we calculated $\Delta\chi^2$, equal to the reduced χ^2 for the four component model minus the reduced χ^2 for the five component model. We also required that the optical depth from the 15.4 μm feature be more than 0.05, a limit set by the IRS flat field uncertainty. This corresponds to a column density for the 15.4 μm CO₂ ice component of $N_{\text{col}}(\text{shoulder}) \approx 0.5 \times 10^{17} \text{ cm}^{-2}$.

We illustrate our YSO selection in Figure 11 where we plot $\Delta\chi^2$ vs. $N_{\text{col}}(\text{shoulder})$. We conclude that a GC source is a YSO if $\Delta\chi^2 \geq 2$ and $N_{\text{col}}(\text{shoulder}) \geq 0.5 \times 10^{17} \text{ cm}^{-2}$. We define a GC source as a possible YSO if $0 < \Delta\chi^2 < 2$ and $N_{\text{col}}(\text{shoulder}) \geq 0.5 \times 10^{17} \text{ cm}^{-2}$. We visually inspected possible YSO spectra, and excluded some spectra as clearly non-YSO: these are SSTGC 440424 (weak 15 μm CO₂ absorption), SSTGC 564417 (OH/IR star), SSTGC 619964 (variable star), SSTGC 696367 (OH/IR star), SSTGC 660708 (OH/IR star), SSTGC 732531 (15 μm CO₂ absorption not significantly different between source and background spectra), SSTGC 738126 (weak 15 μm CO₂ absorption). We consider all other GC sources not to be YSOs. These cutoff values of $\Delta\chi^2$ and $N_{\text{col}}(\text{shoulder})$ closely agree with the YSO classifi-

cation that three of us (DA, SR, KS) did by visually inspecting the IRS spectra of all 107 targets.

Our spectroscopic classification of the 107 GC targets is shown in the fifth column of Table 2. We conclude that 16 sources are YSOs (“yes” in the fifth column of Table 2) and 19 sources are possible YSOs (“maybe” in the fifth column of Table 2). The remaining columns in Table 2 show cross-identifications of our IRS sample with earlier photometry-based YSO selections in Felli et al. (2002), Schuller et al. (2006), and Yusef-Zadeh et al. (2009). We describe these cross-identifications in § 4.4.

The strength of the 15.4 μm peak in our sources is similar to that of the well-studied embedded massive YSO W33A (Gerakines et al. 1999). It is ascribed to a Lewis acid-base interaction of CO₂ (the Lewis acid) with CH₃OH (Dartois et al. 1999a). Other species could be acting as a base as well, but CH₃OH is preferred due to its high abundance toward W33A, which is 5%–22% relative to solid H₂O (Dartois et al. 1999b). Two other massive YSOs (AFGL 7009S, AFGL 2136) show a prominent 15.4 μm peak, and indeed these sources have high CH₃OH abundances as well (Dartois et al. 1999b; Gibb et al. 2004). We therefore suggest that the GC YSOs and possible YSOs may also have high solid CH₃OH abundances. Although the origin of the large quantities of CH₃OH in the previously studied massive YSOs is not fully understood (Dartois et al. 1999a), all lines of sight with high solid CH₃OH abundances are associated with star formation, strengthening the argument that the sources studied in this paper are indeed YSOs.

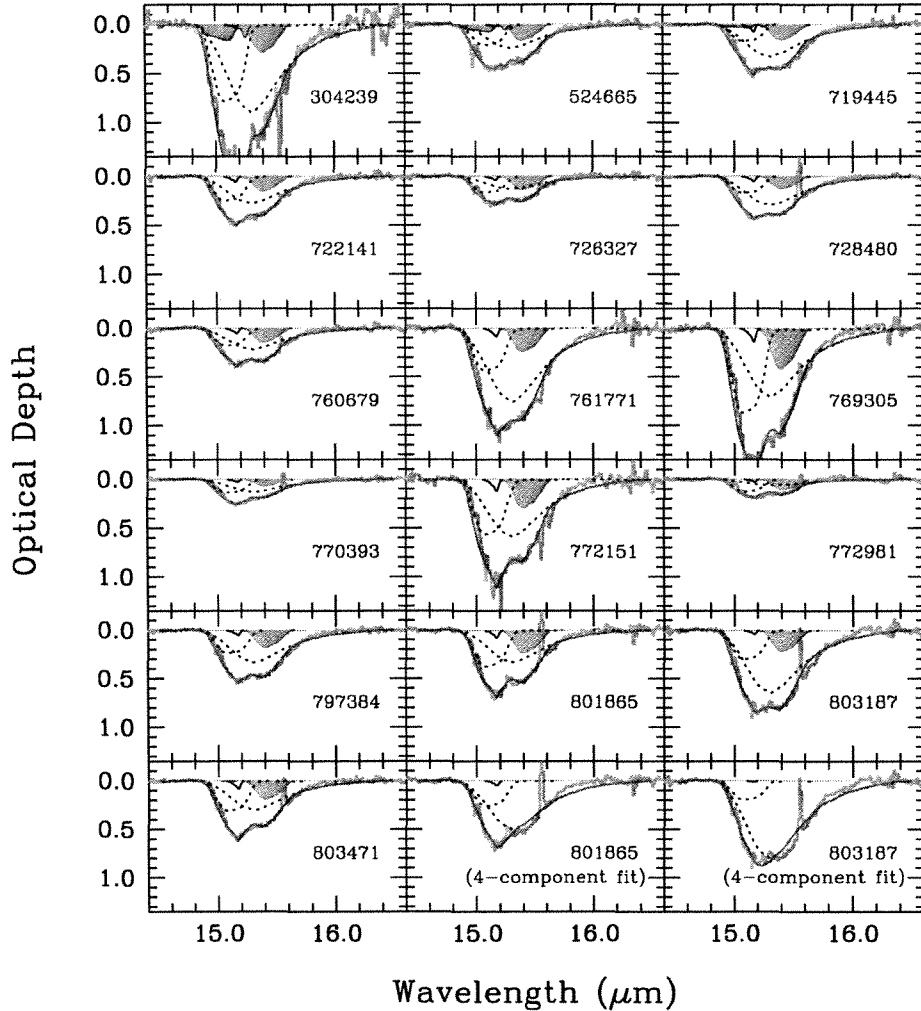


FIG. 8.— Optical depth spectra of spectroscopically identified YSOs centered on the $15\ \mu\text{m}$ CO_2 ice absorption. Best-fitting CO_2 ice models and individual fitting components are displayed for each target: polar (dotted line, centered at $\sim 15.3\ \mu\text{m}$), apolar (dotted line, centered at $\sim 15.1\ \mu\text{m}$), pure (blue shaded), diluted (black solid line), and $15.4\ \mu\text{m}$ shoulder (orange-shaded). Sum of these components is shown as a green line. Bottom two panels show examples of 4-component model fitting without the $15.4\ \mu\text{m}$ shoulder ice.

3.2. Gas-phase Absorption

Many of our YSOs have gas-phase absorption from C_2H_2 ($13.71\ \mu\text{m}$, $\nu_5 = 1-0$), HCN ($14.05\ \mu\text{m}$, $\nu_2 = 1-0$), and/or CO_2 ($14.97\ \mu\text{m}$, $\nu_2 = 1-0$). These gaseous bandheads have been detected toward other massive YSOs, tracing warm and dense gas (e.g., Lahuis & van Dishoeck 2000; Boonman et al. 2003; Knez et al. 2009). All GC sources with these gas absorption bands have been already identified as YSOs through the strength of the $15.4\ \mu\text{m}$ CO_2 ice shoulder, thus strengthening our identification. An AGB star can show either CO_2 gas or C_2H_2 gas but not both, because while O-rich AGB stars sometimes show CO_2 gas in emission or absorption (Justtanont et al. 1998), C_2H_2 gas absorption is found only in C-rich AGB stars (Aoki et al. 1999).

Figure 12 shows relative intensity spectra for the nine YSOs in our sample that show gas-phase absorption from at least one of these species. Three YSOs (SSTGC 524665, SSTGC 797384, SSTGC 803187) presented in A09 are shown in Figure 12 together with six additional YSOs with significant gas-phase absorption. The relative intensity was determined by using a second order polynomial to set a local continuum at $13.30\ \mu\text{m} \leq \lambda \leq 14.55\ \mu\text{m}$ for C_2H_2 and HCN, and

at $14.77\ \mu\text{m} \leq \lambda \leq 15.06\ \mu\text{m}$ for CO_2 .

As in A09, we used model spectra from Cami et al. (2010). These models are based on the HITRAN04 linelist (Rothman et al. 2005) for C_2H_2 and HCN, and based on HITEMP (Rothman et al. 1996) for CO_2 . We did not include isotopes in the computation because of the limited parameter span in the model grids. However, even a relatively high isotopic fraction in the GC ($^{12}\text{C}/^{13}\text{C} \sim 25$; Wannier 1980; Güsten et al. 1985) has a negligible impact on the model fitting. Best-fitting model values of the excitation temperature, T_{ex} , and the gas-phase column density, N_{col} , were found by searching for the minimum χ^2 of the fits over $100\ \text{K} \leq T_{\text{ex}} \leq 1000\ \text{K}$ in steps of $\Delta T_{\text{ex}} = 100\ \text{K}$, and $15 \leq \log N_{\text{col}} \leq 18$ for C_2H_2 , $16 \leq \log N_{\text{col}} \leq 18$ for HCN, and $16 \leq \log N_{\text{col}} \leq 22$ for CO_2 with intervals of 0.1 dex. Errors in these parameters were estimated from $\Delta\chi^2$, where 1σ measurement errors were taken from the scatter in flux. Systematic errors from background subtraction and nodding differences were then added in quadrature. We tested varying covering factors (the fraction of the background continuum source covered by the component in question), but found that the best-fitting value is equal to or close to unity. We adopted a Doppler parameter of 3 km

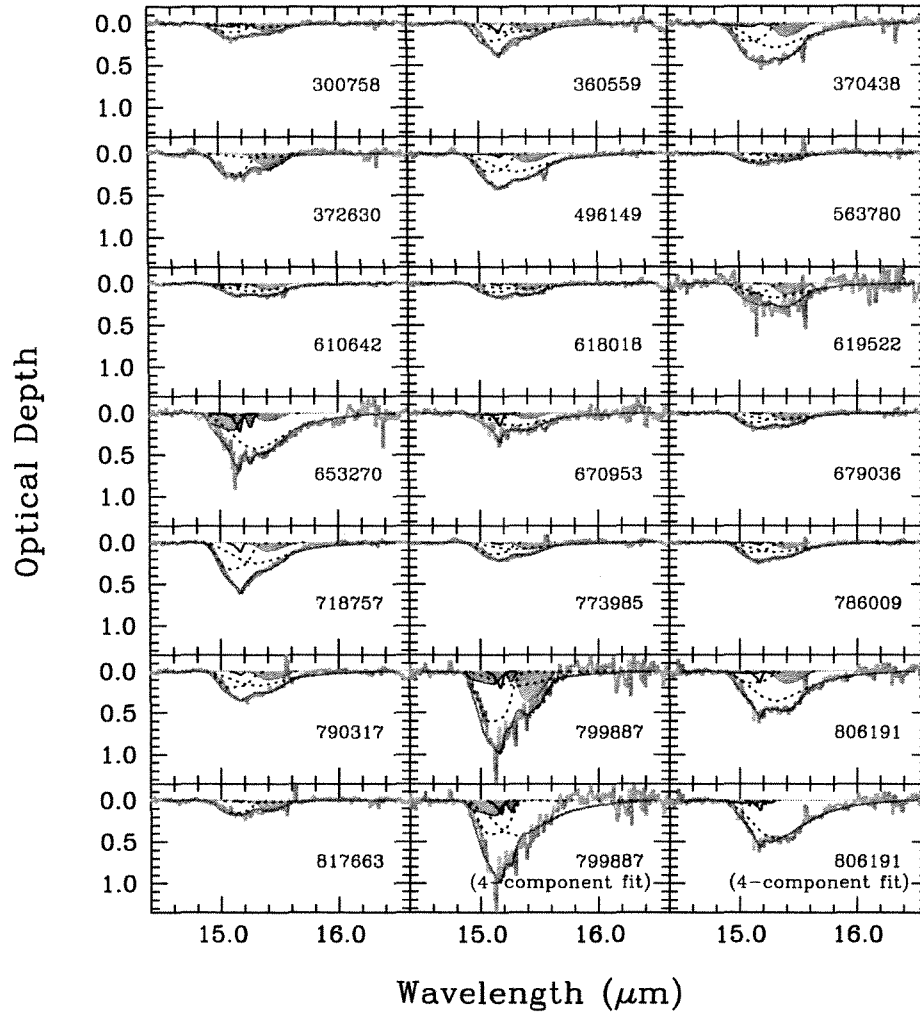


FIG. 9.— Same as in Fig. 8, but for possible YSOs.

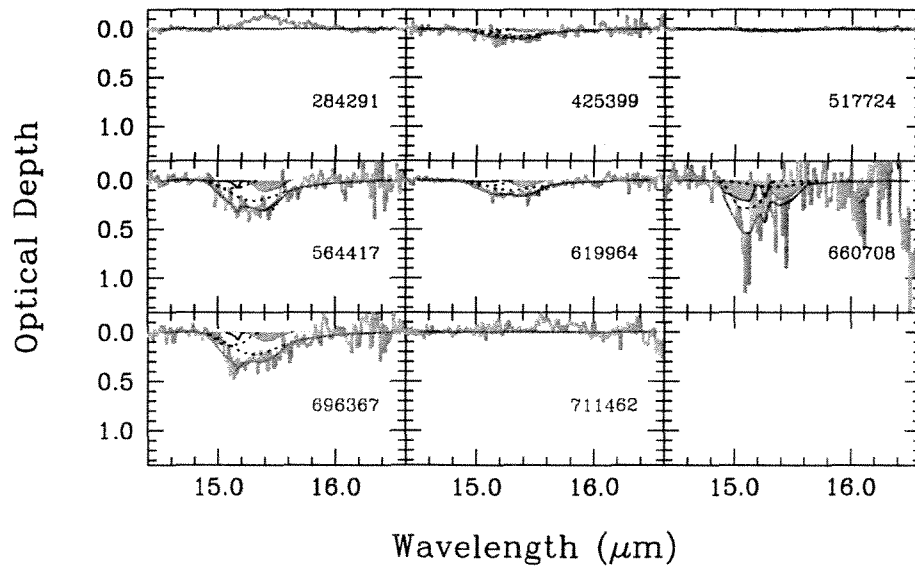


FIG. 10.— Same as in Fig. 8, but for known stars.

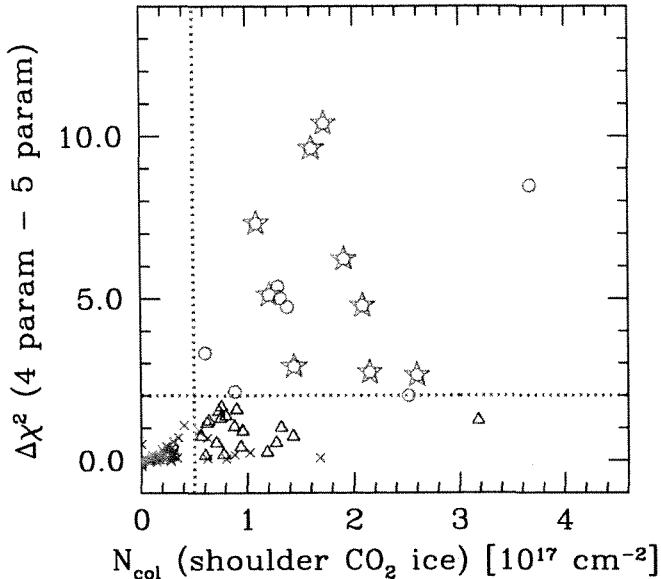


FIG. 11.— Difference ($\Delta\chi^2$) between the reduced χ^2 of the four-component CO₂ ice model (excluding the 15.4 μm shoulder) and the reduced χ^2 of the five-component CO₂ ice model (including the 15.4 μm shoulder) versus the column density of the CO₂ 15.4 μm shoulder component. Two dotted lines represent the criteria for our YSO identification. The YSOs (red circles) have $\Delta\chi^2 \geq 2$ and $N_{\text{col}}(\text{shoulder}) \geq 0.5 \times 10^{17} \text{cm}^{-2}$ and possible YSOs have $N_{\text{col}}(\text{shoulder}) \geq 0.5 \times 10^{17} \text{cm}^{-2}$ and $0 < \Delta\chi^2 < 2$. Red stars mark YSOs with gas-phase absorption features. Possible YSOs are shown as blue triangles and the remaining targets are shown as grey crosses. The value of $\Delta\chi^2$ increases when adding the 15.4 μm shoulder component to the model significantly improves the fit.

s^{-1} .

Figure 12 shows the best-fitting models for each molecular species in red lines. Individual absorption lines are marked with vertical bars if they were identified by three of us (DA, SR, KS) by visually inspecting the IRS spectra of all 107 targets, independent of the model fitting. Some of the lines were marked undetected (e.g., C₂H₂ of SSTGC 761771) because of a low signal-to-noise ratio of its spectrum. The best-fitting model excitation temperatures (T_{ex}) and column densities (N_{col}) of identified lines are listed in Table 5. All objects with identified gas-phase absorptions are selected as YSOs through the detection of the 15.4 μm shoulder component of the 15 μm CO₂ ice absorption feature.

3.3. Extinction

The extinction for our sources can be derived from the optical depths of 9.7 μm and 18 μm silicate absorption features in the IRS spectra. We derived two estimates of the dust extinction: one using the low-resolution modules SL+LL [hereafter $A_V(\text{SL+LL})$], and one using the high-resolution modules SH+LH [hereafter $A_V(\text{SH+LH})$]. The determination of $A_V(\text{SL+LL})$ takes both the 9.7 μm and 18 μm silicate features into account. The high-resolution data do not include the short wavelength side of the 9.7 μm silicate feature, and so $A_V(\text{SH+LH})$ is mainly constrained by the 18 μm silicate feature. The 18 μm feature is broader and shallower than the 9.7 μm absorption, so it provides a weaker constraint on A_V . $A_V(\text{SH+LH})$, however, provides a useful diagnostic when SL is not available, as many sources near Sgr A do not have SL data due to saturation in the peak-up arrays (e.g., SSTGC 610642). Since the high-resolution spectra were scaled to the flux in the

low-resolution modules, $A_V(\text{SL+LL})$ and $A_V(\text{SH+LH})$ are not independent from each other.

To determine the dust extinction, we model the 5 μm – 32 μm spectrum by simultaneously fitting the underlying continuum, the silicate dust features centered at 9.7 μm and 18 μm , and the 13 μm librational H₂O ice absorption (see Figure 4 in A09). The entire silicate extinction curve, derived using the GCS 3 spectrum from the Infrared Space Observatory (ISO) Short Wavelength Spectrometer (SWS) (Kemper et al. 2004), is characterized by the optical depth at 9.7 μm , $\tau_{9.7}$. We adopted the laboratory spectrum of pure amorphous H₂O ice at $T = 10$ K (Hudgins et al. 1993) to model the 13 μm librational H₂O absorption. This shallow absorption is not well-constrained, however, so that the resulting column density of H₂O ice, $N_{\text{col}}(13 \mu\text{m})$, is uncertain. We used a second-order polynomial to simulate the overall shape of the SED plus grey extinction in the absence of silicate and H₂O absorption. Before performing this non-linear least squares fit (Markwardt 2009) we masked molecular absorption features at $5.5 \mu\text{m} < \lambda \lesssim 7.5 \mu\text{m}$, PAH emission at $\sim 11.3 \mu\text{m}$, CO₂ ice absorption at $\sim 15 \mu\text{m}$, strong emission lines, as well as the noisy bottom part of the 9.7 μm silicate feature ($9.3 \mu\text{m} < \lambda < 10.1 \mu\text{m}$). We derived $A_V(\text{SL+LL})$ from $\tau_{9.7}$ by adopting $A_V/\tau_{9.7} = 9$ (Roche & Aitken 1985), the value measured for lines of sight towards the GC. We derived $A_V(\text{SH+LH})$ in the same way, except that we modeled the 10 μm – 32 μm high-resolution spectra instead.

The uncertainties in $A_V(\text{SL+LL})$ and $A_V(\text{SH+LH})$ are dominated by the uncertainty in choosing the continuum. We estimated these uncertainties by comparing results where the continuum was derived from the same wavelength regions in all spectra to results where each continuum was set interactively. Applying a second-order polynomial for a continuum generally results in a good fit over $10 \mu\text{m} \lesssim \lambda \lesssim 32 \mu\text{m}$, but underestimates fluxes at $< 8 \mu\text{m}$, which may be due to under-subtraction of background PAH emission at $\sim 7.7 \mu\text{m}$. We followed the prescription in Boogert et al. (2008) to force the continuum to match (by eye) the observed flux at $\sim 5.5 \mu\text{m}$ and $\sim 7.5 \mu\text{m}$ and to set an approximate flux at $\sim 30 \mu\text{m}$. We tried a number of interactive continuum settings, but this approach generally results in a much worse agreement of the model fits with observed flux over $10 \mu\text{m} \lesssim \lambda \lesssim 32 \mu\text{m}$. We took this as an upper 1σ boundary of $A_V(\text{SL+LL})$. Errors in $A_V(\text{SH+LH})$ include statistical uncertainties, where we took the scatter of points at $20 \mu\text{m} \leq \lambda \leq 30 \mu\text{m}$ with respect to a second-order polynomial as the flux errors over the entire wavelength range, added in quadrature to uncertainties from varying the background subtraction and uncertainties between the two nod positions.

Table 6 shows $A_V(\text{SL+LL})$ and $A_V(\text{SH+LH})$ estimates for YSOs and possible YSOs. We compare these two extinction estimates in the upper panel of Figure 13. The extinction for each YSO is a combination of extinction along the line of sight to the GC and extinction intrinsic to the YSO; sources which are not YSOs will not always have intrinsic extinction. There is a good correlation between $A_V(\text{SL+LL})$ and $A_V(\text{SH+LH})$ as illustrated in Figure 13. This is expected, because the high-resolution spectra are scaled to the low-resolution spectra, and so the two methods are not completely independent from each other. The weighted mean difference is $\langle A_V(\text{SH+LH}) - A_V(\text{SL+LL}) \rangle = +0.38 \pm 0.65$ mag for both YSOs and possible YSOs. The (unweighted) rms difference is 11 mag, compared to the formal uncertainties of ~ 9 mag from both axes.

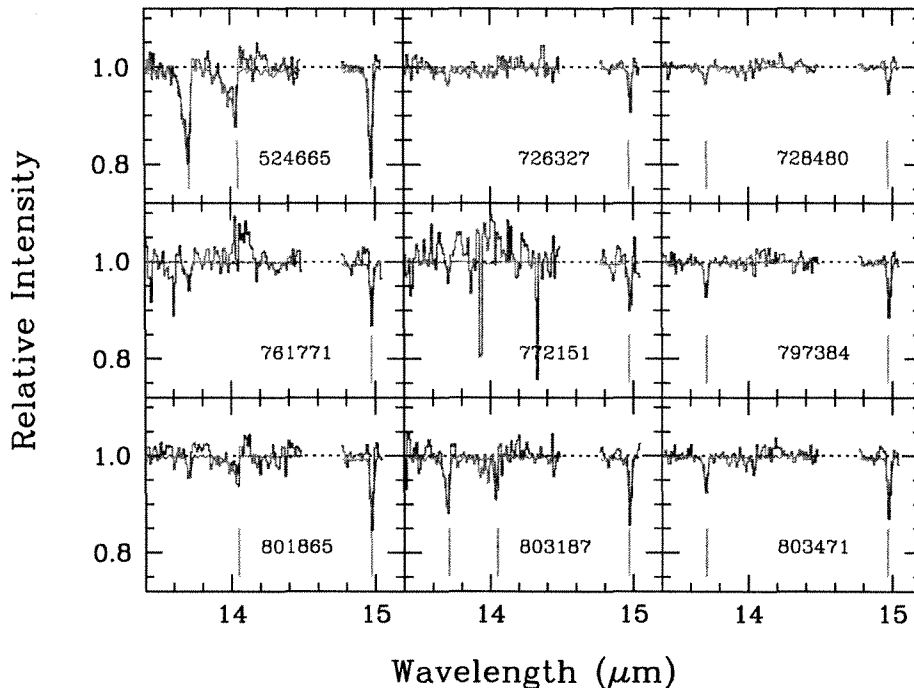


FIG. 12.— Gas-phase molecular absorptions from $\text{C}_2\text{H}_2 \nu_5 = 1-0$ (13.71 μm), $\text{HCN} \nu_2 = 1-0$ (14.05 μm), and $\text{CO}_2 \nu_2 = 1-0$ (14.97 μm). These gas-phase molecular features trace warm and dense gas detected towards galactic massive YSOs. Red lines represent models with best-fitting T_{ex} and N_{col} (see text). Individual absorption lines are marked with vertical bars if they were identified, independent of the model fitting. All objects with identified gas-phase absorptions are selected as YSOs through the detection of the 15.4 μm shoulder component of the 15 μm CO_2 ice absorption feature.

The lower panel in Figure 13 shows a comparison of A_V (SL+LL) to A_V (foreground) derived from the extinction map in Schultheis et al. (2009). The latter is based on the 2MASS and IRAC color-magnitude diagrams of GC red giant branch stars within 2' from each source. The errors are the rms difference of A_V (foreground) derived at the positions of four background pointings. As seen in the figure, A_V (SL+LL) is systematically larger than A_V (foreground) for YSOs and possible YSOs. Such overall behavior is expected for YSOs, since A_V (foreground) from Schultheis et al. (2009) is a spatially averaged line-of-sight extinction to the GC, while A_V (SL+LL) is the sum of the line-of-sight extinction to the GC and the localized extinction from the dusty envelope of the YSO.

3.4. Molecular Abundances

By using the dust extinction values derived in the previous section, we derived abundances for gas-phase molecular absorbers with respect to hydrogen. We obtained a total hydrogen column density from the optical depth of the 9.7 μm silicate absorption, assuming $A_V/\tau_{9.7} = 9$ (Roche & Aitken 1985) and $N_{\text{H}}/A_V \approx 1.87 \times 10^{21} \text{ cm}^{-2} \text{ mag}^{-1}$ (Bohlin et al. 1978) at $R_V = 3.1$. We used A_V (SL+LL) to derive the H_2 column density, assuming $N_{\text{H}_2} = N_{\text{H}}/2$. Here we implicitly assumed that the H_2 column density along the full 8 kpc line of sight is comparable to the local value near the YSO. A factor of two difference would exist, if the local and the full H_2 column densities are the same, but we neglected this difference.

The gas-phase molecular abundances relative to H_2 (i.e., ratios of column densities) are shown in Table 5. Our derived abundances for C_2H_2 and HCN are $10^{-6.9}$ – $10^{-5.3}$, and our gas-phase CO_2 abundances are $10^{-6.4}$ – $10^{-5.1}$. Intervening molecular clouds in the line of sight to the GC are less likely the main cause of these absorptions because the average HCN abundance of 2.5×10^{-8} towards Sgr B2(M) (Greaves & Nyman

1996), where half of our YSOs and possible YSOs are found (§ 4.3), is an order of magnitude lower than our measurements.

Individual gas-phase abundances are comparable to or generally higher than those in earlier studies. Lahuis & van Dishoeck (2000) found abundances of 10^{-8} – 10^{-6} for C_2H_2 and HCN in the warm gas for several massive YSOs, and Knez et al. (2009) found $10^{-6.1}$ for C_2H_2 and $10^{-8.3}$ for HCN towards IRS 1 in NGC 7538. Boonman et al. (2003) estimated CO_2 abundances of $10^{-7.2}$ – $10^{-6.5}$ towards lines of sight to several YSOs. However, these differences could be due to the uncertainties of comparing different techniques of deriving $N(\text{H}_2)$. If we consider the column densities of warm gas towards massive YSOs, our values are in good agreement with those found in the previous work (Lahuis & van Dishoeck 2000; Boonman et al. 2003; Knez et al. 2009). In addition, our gas to solid abundance ratios for CO_2 (10^{-1} – 10^{-2}), which do not require knowledge of the foreground extinction, are consistent with Boonman et al. (2003).

4. PROPERTIES OF MASSIVE YSOS IN THE GC

In the above section, we spectroscopically identified 16 YSOs and 19 possible YSOs from among 107 IRS targets in the GC. Although our selection of massive YSOs is primarily based on the 15 μm CO_2 ice absorption profile, absorption from hot and dense molecular gases further supports our selection procedures. In this section, we derive and inspect properties of these YSOs and possible YSOs using SED model fits, and look for a spatial correlation of these sources in the CMZ.

4.1. YSO Parameters from SED Fitting

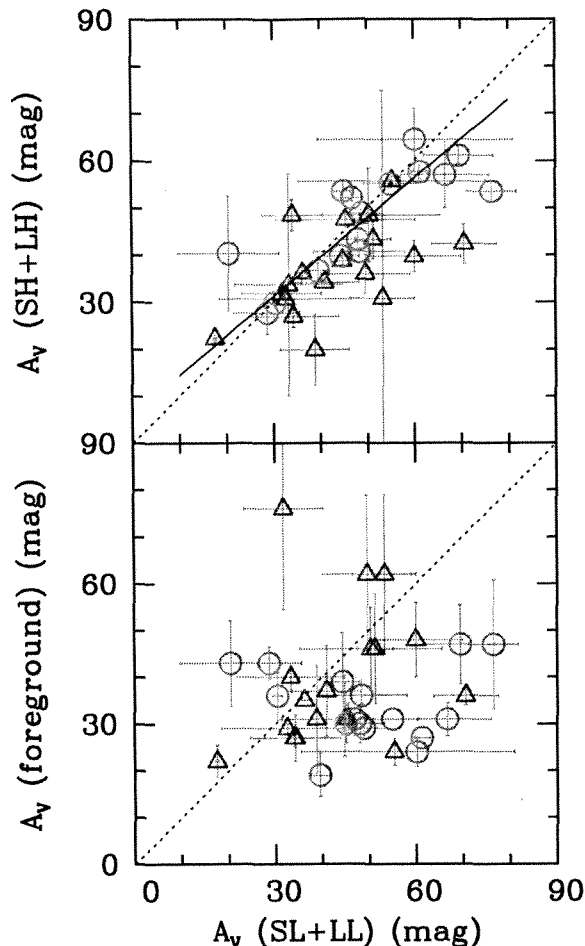


FIG. 13.— Comparisons of A_V (SL+LL) with A_V (SH+LH) (*top*) and with those based on the colors of giant stars in the field (Schultheis et al. 2009) (*bottom*). Red circles are YSOs, and blue triangles are possible YSOs selected in this work. Dotted line represents equal values for A_V (SL+LL) and A_V (SH+LH). Solid line in the *top* panel shows a linear fit to the data using errors in both axes. A_V (SL+LL) is systematically larger than A_V (foreground) as A_V (SL+LL) is the sum of the line-of-sight extinction and the localized extinction from the dusty envelope of a YSO while A_V (foreground) is a spatially averaged line-of-sight extinction.

For our 35 YSOs and possible YSOs, we performed SED fitting using a set of models in Robitaille et al. (2006). For this purpose, we used the *Online SED Fitter*¹¹ (Robitaille et al. 2007) to derive YSO parameters, such as the mass of the central object, the bolometric luminosity, and the accretion rate from the envelope.

As an input to the *SED Fitter*, we used available near- and mid-IR photometry as listed in Table 7. The near-IR *JHK* observations are *Aperture3* magnitudes from UKIDSS DR2 (Warren et al. 2007). Many of our YSOs and possible YSOs are found on saturated pixels on the MIPS 24 μm images (Carey et al. 2009). Therefore, we derived synthetic photometry at 24 μm by convolving the MIPS [24] filter response function on the IRS spectra, following the prescriptions on the *Spitzer* website¹². These values are listed in Table 7. Synthetic values for our IRS targets are 1.05 ± 0.17 mag ($N_{\text{comp}} = 29$) systematically smaller (brighter) than MIPS [24] photometry (S. Carey, 2008, private communication).

¹¹ <http://caravan.astro.wisc.edu/protostars>

¹² See <http://ssc.spitzer.caltech.edu/dataanalyisistools/cookbook/10/>.

Similarly, we found a mean difference of 0.72 ± 0.09 mag ($N_{\text{comp}} = 77$) between IRAC [8.0] photometry (Ramírez et al. 2008) and synthetic values. Again the sense of the difference is that synthetic values are brighter than Ramírez et al. values. This is likely due to extended emission around YSOs. We also utilized 450 μm and 850 μm observations from the Submillimetre Common User Bolometer Array (SCUBA; Di Francesco et al. 2008), measured with a 23'' diameter beam.

In addition to the above photometry, we derived monochromatic fluxes at 14 wavelength points: 5.58 μm , 6.4 μm , 7.65 μm , 8.5 μm , 9.0 μm , 9.7 μm , 11.0 μm , 12.0 μm , 13.5 μm , 17.0 μm , 18.0 μm , 21.0 μm , 30.0 μm , and 35.0 μm . These points were selected to characterize the overall shape of a SED with as little ice features as possible, because the models do not include ices. We computed a monochromatic flux with a 2%-wide Gaussian filter in these wavelength points, except at 9.7 μm where we used a 3%-wide filter, to better characterize the bottom of the silicate absorption band. Note that we did not use the IRAC [5.8] and [8.0] photometry and instead used the above synthetic values to avoid strong 6 μm and 7 μm absorption bands, which are not included in the models.

For each source, we ran the *Online SED Fitter* using the above set of photometry and collected results that satisfy $(\chi^2 - \chi^2_{\text{min}})/N_{\text{tot}} < 5$, where χ^2_{min} is the minimum χ^2 value from the available model sets, and N_{tot} is the total number of data points, which are between 12 and 22 for our sources. We note that the fitting is not strictly statistical, given the limited parameter space of models for all 14 YSO parameters (see Robitaille et al. 2007). We chose the above cut to include reasonable fitting results, and then estimated a mean and a standard deviation for each YSO parameter.

Figure 14 displays SED fitting results overplotted on the input photometry for four YSOs. All 35 YSOs and possible YSOs are shown in the online journal. The black solid line shows a best-fitting SED, and grey lines show acceptable fits from the on-line SED fitter. The dashed line represents the emission from the central source in the absence of extinction from the dusty envelope. In this fitting exercise, we restricted the source distance, d , to $7 \text{ kpc} \leq d \leq 9 \text{ kpc}$ from the Sun, and interstellar extinction along the line of sight to the GC to $20 \text{ mag} \leq A_V \leq 40 \text{ mag}$.

Figure 15 shows results for derived YSO parameters, and Table 8 summarizes the results. Entries with no error bars indicate that a single solution is found within $(\chi^2 - \chi^2_{\text{min}})/N_{\text{tot}} < 5$. Our derived masses of central objects span $8 M_{\odot} \lesssim M_* \lesssim 23 M_{\odot}$, and the total luminosities range over $10^3 L_{\odot} \lesssim L_{\text{tot}} \lesssim 10^5 L_{\odot}$. Note that the mass is not directly determined from the SED; rather, it is the bolometric luminosity and the temperature we are determining, and the mass is implicitly constrained by these from the evolutionary tracks built-in to the model grid. The mass accretion rate from the envelope is another indicator for the evolutionary stage of YSOs. For our YSOs and possible YSOs, we found a heavy infall rate, $10^{-4} M_{\odot} \text{ yr}^{-1} \lesssim \dot{M}_{\text{env}} \lesssim 10^{-3} M_{\odot} \text{ yr}^{-1}$, which is consistent with those for Stage-I YSOs (Robitaille et al. 2006). The range of these parameters recovered from the *SED fitting tool* remained essentially unchanged if we instead imposed a A_V limit using A_V (foreground) measurements in Table 6 with its $\pm 2\sigma$ error bounds (Schultheis et al. 2009). Our SED fitting suggests that our sources are massive YSOs in their early stages of protostar evolution.

Figure 16 shows the color distribution of YSOs and possible

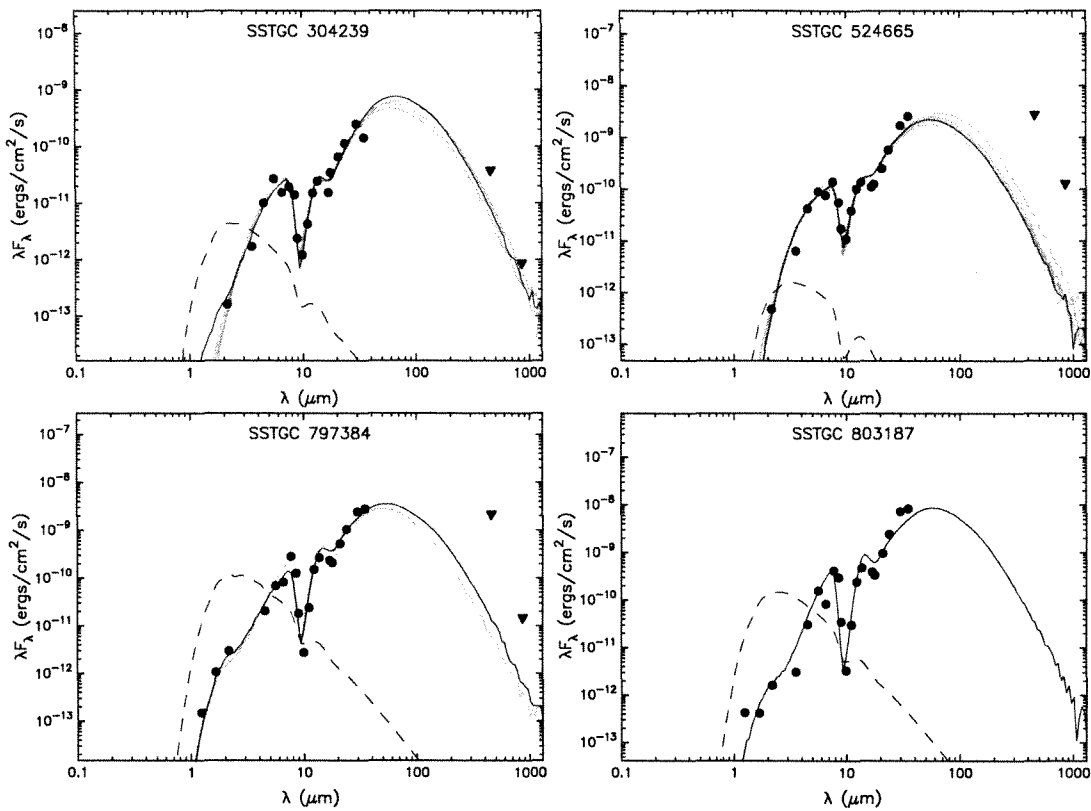


FIG. 14.— SED fitting results for four GC YSOs using a set of models in Robitaille et al. (2006) and based on near-infrared photometry, synthetic values derived from the IRS spectra, and SCUBA observations (Table 7). Observed points are shown as filled circles and upper limits are shown as downward pointing triangles. The black line is a best-fitting model, and grey lines represent acceptable fits. Dashed line is the emission from the central object in the absence of the dusty envelope. The SED model fitting suggests that our spectroscopically selected YSOs are massive Stage-I YSOs. (An extended version of this figure is available in the online journal, showing all 35 GC YSOs and possible YSOs.)

YSOs in the mid-IR color-color diagrams, overlaid with regions occupied by theoretical Stage-I objects (Robitaille et al. 2006). The colors of YSOs and possible YSOs, relative to non-YSOs, are a bit bluer for [5.8]-[8.0]. On the other hand, YSOs and possible YSOs are redder in [3.6]-[4.5] and [3.6]-[5.8]. All of our 107 sources have similar [8.0]-[24] colors. Although YSOs and possible YSOs in the GC have colors that are similar to the theoretically predicted colors, non-YSOs are also found in the same color space. This confirms earlier theoretical work (e.g., Robitaille et al. 2007), concluding that broad-band colors are not sufficient to separate YSOs from non-YSOs.

4.2. Mass Estimates from Radio Continuum

Eight YSOs and possible YSOs are coincident with radio continuum sources, and are thus likely to be compact H II regions. These are listed in the last two columns of Table 8. We used radio continuum data (Zoonematkermani et al. 1990; Mehringer et al. 1992, 1993; Becker et al. 1994; Mehringer 1995; Lazio & Cordes 1998; Yusef-Zadeh et al. 2004; White et al. 2005; Lazio & Cordes 2008; Yusef-Zadeh et al. 2009) to derive the number of ionizing photons for each H II region, assuming a distance of 8 kpc. We then converted the number of ionizing photons to stellar mass by using the results of Panagia (1973) and assuming a surface gravity of $\log g = 4.2$. Our derived masses, listed in Table 8, agree on average with those estimated from SED fits in the previous section (§ 4.1).

4.3. Spatial Distribution of YSOs in the GC

We confined our spectroscopic sample to those within $|b| < 15'$ to avoid likely foreground objects (§ 2.1). Nevertheless, this spatial cut is generous enough that our spectroscopic survey is almost free from a spatially dependent sample bias, and enables us to map out active star-forming regions in the GC and to study their relation to the interstellar medium (ISM).

Figure 17 displays the locations of 35 YSOs and possible YSOs in the CMZ (see Figure 1 for the locations of all of our spectroscopic targets). Although YSOs and possible YSOs are found throughout the CMZ, it is striking to see that half of these sources (18 out of 35) are found in and around Sgr B. Sgr B is known as the most active star-forming region in the Galaxy (Bally et al. 2010), but this is the first direct evidence of the presence of YSOs in this region at the earliest stage of star formation ($\lesssim 1$ Myr). Figure 18 shows the Sgr B region with locations of our YSOs and possible YSOs. As seen on the $24 \mu\text{m}$ map, our sources are preferentially found on the edge of strong $24 \mu\text{m}$ emission regions.

4.4. Star Formation Rate at the GC

YSOs are direct tracers of early star formation, and can be used to estimate the *in situ* star formation rate (SFR) in the GC. Previous identifications of YSOs based on broad-band photometry were used to infer the SFR in the GC, but the heavy extinction towards the GC limits any estimate of the SFR based on photometrically selected YSOs. This is because reddened AGB stars have similar colors (e.g., Figure 16). Our IRS spectra provide a unique opportunity to check how well earlier studies selected their YSO candidates, and can be used to refine SFR estimates at the GC.

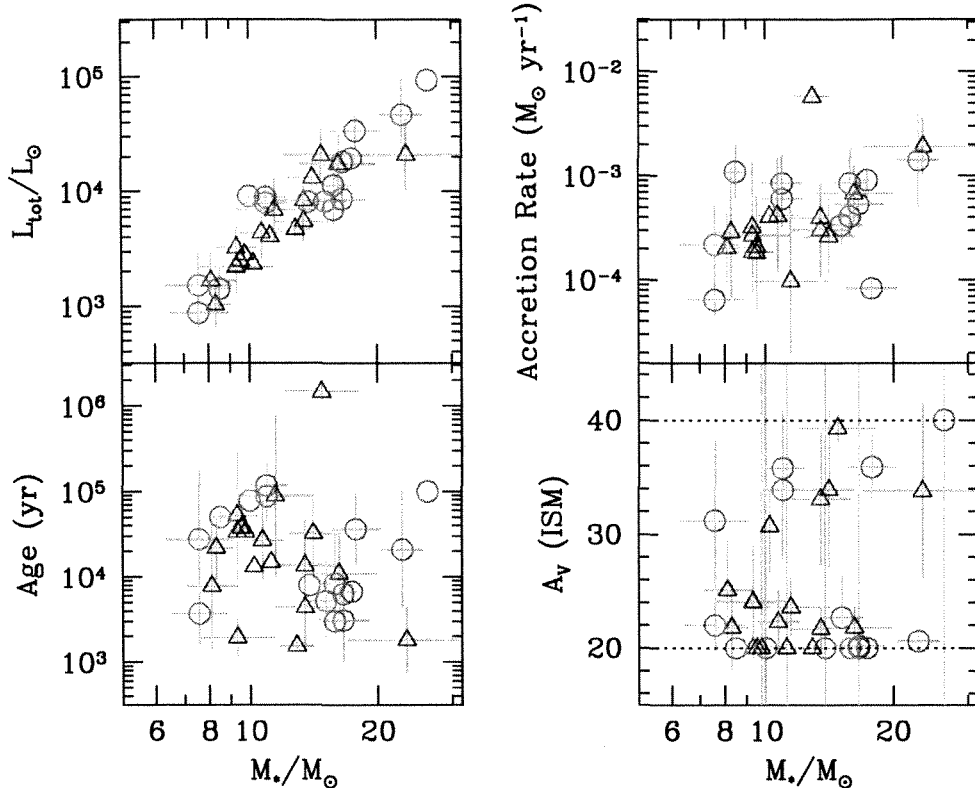


FIG. 15.— SED fitting results for YSOs (red circles) and possible YSOs (blue triangles) in our sample. The total luminosity, age, envelope accretion rate, and foreground extinction (from the top left to the bottom right panels) are shown as a function of the mass for a central object.

Table 2 includes cross-identifications of our IRS sample with earlier photometry-based YSO selections in Felli et al. (2002), Schuller et al. (2006), and Yusef-Zadeh et al. (2009). YSO selections in both Felli et al. (2002) and Schuller et al. (2006) are based on ISOGAL photometry (Omont et al. 2003; Schuller et al. 2003), while that of Yusef-Zadeh et al. (2009) is based on the *Spitzer* IRAC (Ramírez et al. 2008) and MIPS photometry (Hinze et al. 2009). The source catalogs (Omont et al. 2003; Schuller et al. 2003; Hinze et al. 2009) do not cover the entire CMZ, in particular near Sgr A. Sources with missing data (“...”) in Table 2 represent our spectroscopic targets that were not detected in these catalogs in a 3'' search radius.

Felli et al. (2002) used ISOGAL photometry at 7 μm and 15 μm to select bright YSO candidates, using the mid-infrared color-magnitude diagram for ultra-compact H II regions. In total, 28 sources identified by Felli et al. (2002) as photometric YSOs (“yes” in column 6 of Table 2) were cross-matched with our IRS targets (Table 2, column 5) in a 3'' search radius, but we identified only 36% of them (10/28) as YSOs (4) or possible YSOs (6) in our study.

YSO candidates were also selected by Schuller et al. (2006) based on ISOGAL photometry at 7 μm and 15 μm and spatial extent of ISOGAL sources. Their study focused on a small 20' \times 20' field between Sgr A and Sgr C. We have obtained IRS spectra of only eight ISOGAL sources in this field. Schuller et al. (2006) photometrically identified five GC sources as YSOs (Table 2, column 7). However, none of them are identified by us as YSOs or possible YSOs (Table 2, column 5). The low rate in the YSO identification could be due to their selection criteria based on the spatial extent of

sources, while our spectroscopic targets were selected from point sources in the IRAC bandpasses (§ 2.1).

A comparable hit rate to that from Felli et al. (2002) was found for YSO candidates from the most recent photometric study by Yusef-Zadeh et al. (2009), whose YSO candidates were identified based on the *Spitzer* IRAC and MIPS images. In total 17 photometric YSOs (“yes” in Table 2, column 8) in their list were cross-matched with our IRS targets in a 3'' search radius, but only 47% (8/17; “yes” in Table 2, column 8) of them were found to be either YSOs (3) or possible YSOs (5) in our study.

A complete analysis on the SFR estimate requires a better understanding of the sample bias in our spectroscopic target selection, which is the subject of the next papers of this series. Nonetheless, we can make a preliminary estimate on the SFR based on the result in this paper: since the hit rate of the photometric YSO selection in Yusef-Zadeh et al. (2009) is $\sim 50\%$, their SFR estimate for Stage I YSOs would have been overestimated by a factor of ~ 2 . They have concluded that the Stage I SFR is $\sim 0.14 M_{\odot} \text{ yr}^{-1}$, so this implies a revised SFR $\sim 0.07 M_{\odot} \text{ yr}^{-1}$ at the GC. If we assume a gas surface density of the GC from the total mass of $5.3 \times 10^7 M_{\odot}$ (Pierce-Price et al. 2000) over the entire CMZ, both values of the star formation rate are roughly consistent with the Kennicutt-Schmidt law (Kennicutt 1998).

5. SUMMARY

We obtained *Spitzer*/IRS spectra for 107 sources in the GC, which were selected based on near- and mid-IR photometry including those obtained from *Spitzer*/IRAC. Based on the shape of the 15 μm CO₂ spectral feature and the strength

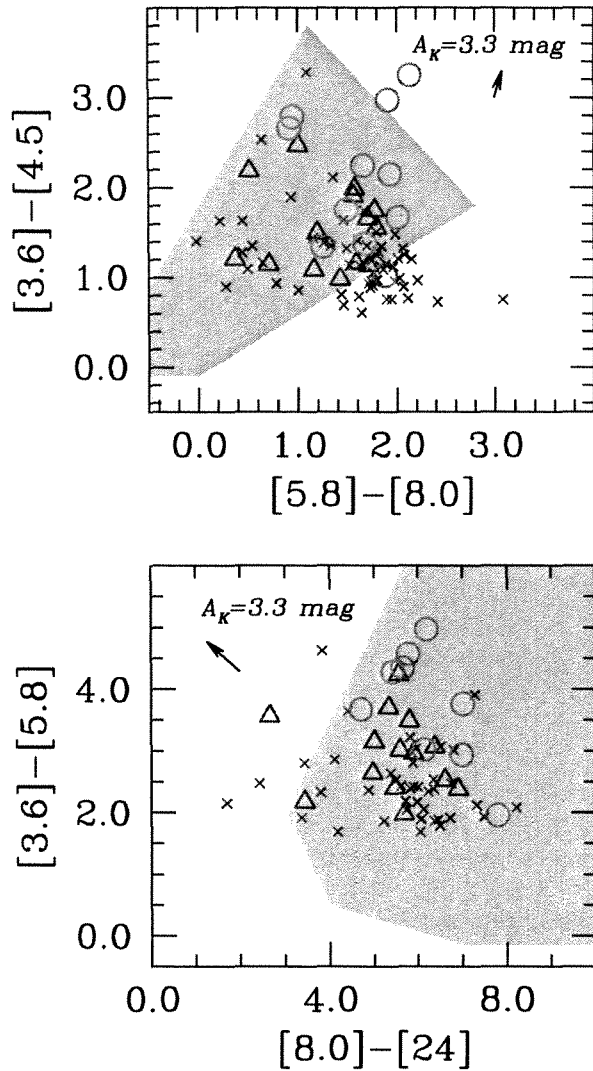


FIG. 16.— Distribution of YSOs (red circles) and possible YSOs (blue triangles) on IRAC/MIPS color-color diagrams. Grey crosses represent our remaining IRS targets. Grey regions are theoretically predicted color ranges for Stage-I YSOs (adapted from Robitaille et al. 2006). Photometry is not corrected for extinction. The arrows indicate the reddening vector from the extinction law in Chiar & Tielens (2006) at $A_K = 3.28$ mag or $A_V = 29$ mag (Figer et al. 1999). There is significant overlap between YSOs and non-YSOs in our sample within the predicted colors of Stage-I YSOs.

of the $15.4 \mu\text{m}$ shoulder CO_2 ice component, we selected 35 YSOs and possible YSOs. Our identifications are further supported by the presence of hot and dense gas-phase molecular absorptions such as C_2H_2 , HCN, and CO_2 for some YSOs. This is the first spectroscopic identification of a large YSO population, tracing an early stage of star formation in the GC. Spectroscopic confirmation of candidate YSOs in the GC is essential because the older stellar population in the GC, when reddened by $A_V \sim 30$, has infrared colors similar to those of YSOs.

From the SED model fitting, we inferred that the masses of these objects are typically $\sim 8 - 23 M_\odot$, and that the high infall rate from the envelope suggests that they are on Stage I, an early evolutionary stage of protostars (e.g., Robitaille et al. 2006). We found that these YSOs and possible YSOs are found throughout the whole CMZ, but half of them are located in and around the Sgr B. We found that about 50% of photometrically selected YSOs are spectroscopically confirmed by our study. We estimated a preliminary star formation rate, based on an earlier photometric study by Yusef-Zadeh et al. (2009), to be $\sim 0.07 M_\odot \text{ yr}^{-1}$.

Our *Spitzer*/IRS survey is limited to YSOs of at least $\sim 3 M_\odot$ (masses of central objects). However, next generation telescopes, such as the Giant Magellan Telescope (GMT) or the James Webb Space Telescope (JWST), will overcome this limit, exploring significantly less massive stars with high-resolution imaging and moderate/high-resolution spectroscopic capabilities in the near- and mid-IR range, allowing detailed studies of the initial mass function in these crowded fields. Until then, our *Spitzer*/IRS data will remain as a unique database for studying the star formation process in the GC.

We thank the referee for careful and detailed comments. This work is based on observations made with the *Spitzer Space Telescope*, which is operated by the Jet Propulsion Laboratory, California Institute of Technology under a contract with NASA. Support for this work was provided by NASA through an award issued by JPL/Caltech. This research has made use of the SIMBAD database, operated at CDS, Strasbourg, France.

REFERENCES

- An, D., et al. 2009, *ApJ*, 702, L128 (A09)
Aoki, W., Tsuji, T., & Ohnaka, K. 1999, *A&A*, 350, 945
Bally, J., et al. 1987, *ApJS*, 65, 13
Bally, J., Stark, A. A., Wilson, R. W., & Henkel, C. 1988, *ApJ*, 324, 223
Bally, J., et al. 2010, *ApJ*, 721, 137
Becker, R. H., White, R. L., Helfand, D. J., & Zoonematkermani, S. 1994, *ApJS*, 91, 347
Bergin, E. A., Melnick, G. J., Gerakines, P. A., Neufeld, D. A., & Whittet, D. C. B. 2005, *ApJ*, 627, L33
Bohlin, R. C., Savage, B. D., & Drake, J. F. 1978, *ApJ*, 224, 132
Boogert, A. C. A., et al. 2008, *ApJ*, 678, 985
Boonman, A. M. S., van Dishoeck, E. F., Lahuis, F., & Doty, S. D. 2003, *A&A*, 399, 1063
Cami, J., van Malderen, R., & Markwick, A. J. 2010, *ApJS*, 187, 409
Carey, S. J., et al. 2009, *PASP*, 121, 76
Chiar, J. E., & Tielens, A. G. G. M. 2006, *ApJ*, 637, 774
Churchwell, E., Babler, B. L., Meade, M. R., Whitney, B. A., Benjamin, R., Indebetouw, R., Cyganowski, C., Robitaille, T. P., Povich, M., Watson, C., Bracker, S. 2009, *PASP*, 121, 213
Dartois, E., Demyk, K., d'Hendecourt, L., & Ehrenfreund, P. 1999a, *A&A*, 351, 1066
Dartois, E., Schutte, W., Geballe, T. R., Demyk, K., Ehrenfreund, P., & d'Hendecourt, L. 1999b, *A&A*, 342, L32
Di Francesco, J., Johnstone, D., Kirk, H., MacKenzie, T., & Ledwosinska, E. 2008, *ApJS*, 175, 277
Ehrenfreund, P., et al. 1999, *A&A*, 350, 240
Fatuzzo, M., & Melia, F. 2009, *PASP*, 121, 585
Fazio, G. G., et al. 2004, *ApJS*, 154, 10
Felli, M., Testi, L., Schuller, F., & Omont, A. 2002, *A&A*, 392, 971
Figer, D. F., et al., 1999, *ApJ*, 525, 750
Frogel, J. A., & Whitford, A. E., 1987, *ApJ*, 320, 199
Gerakines, P. A., Schutte, W. A., Greenberg, J. M., & van Dishoeck, E. F. 1995, *A&A*, 296, 810
Gerakines, P. A., et al. 1999, *ApJ*, 522, 357
Gibb, E. L., Whittet, D. C. B., Boogert, A. C. A., & Tielens, A. G. G. M. 2004, *ApJS*, 151, 35
Greaves, J. S., & Nyman, L.-A. 1996, *A&A*, 305, 950
Güsten, R., Henkel, C., & Batrla, W. 1985, *A&A*, 149, 195
Hinz, J. L., Rieke, G. H., Yusef-Zadeh, F., Hewitt, J., Balog, Z., & Block, M. 2009, *ApJS*, 181, 227
Houck, J. R., et al. 2004, *ApJS*, 154, 18
Hudgins, D. M., Sandford, S. A., Allamandola, L. J., & Tielens, A. G. G. M. 1993, *ApJS*, 86, 713

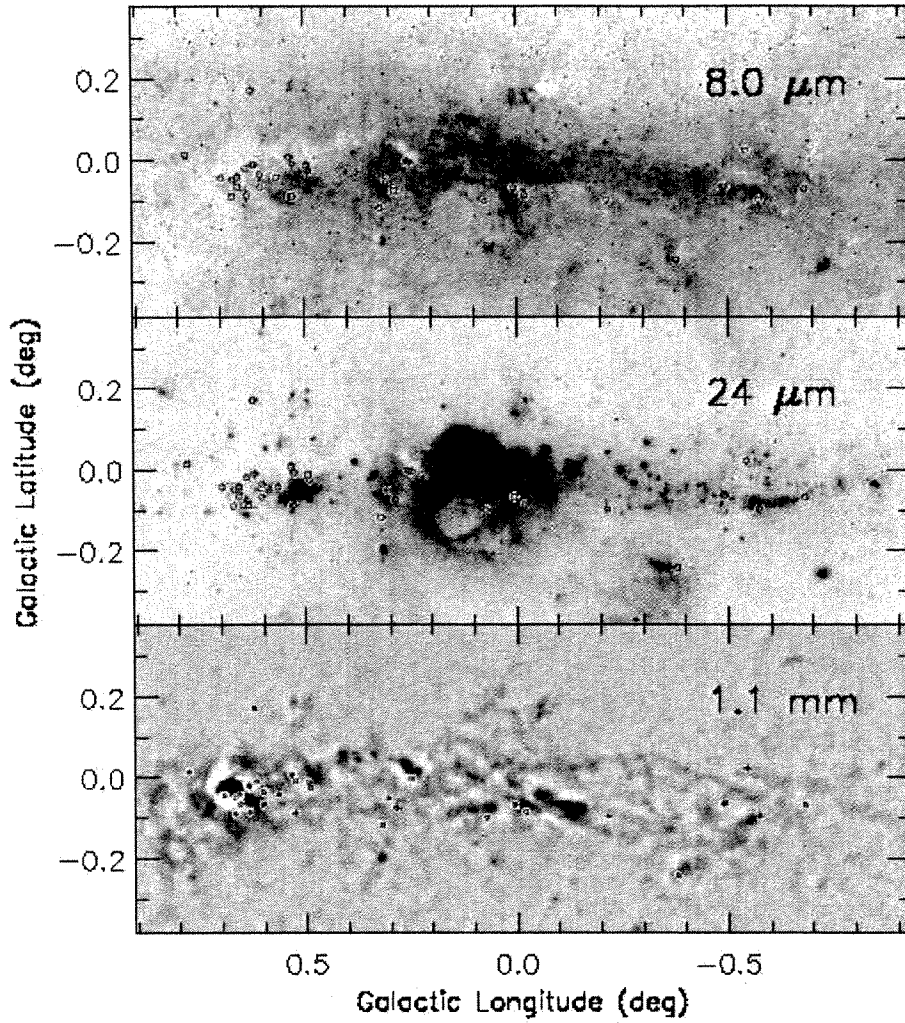


FIG. 17.— Spatial distribution of 35 YSOs and possible YSOs on images from *Spitzer*/IRAC $8\ \mu\text{m}$ (Stolovy et al. 2006, top), MIPS $24\ \mu\text{m}$ combined with images from Midcourse Space Experiment (MSX) $21.34\ \mu\text{m}$ E band (Yusef-Zadeh et al. 2009, middle), and $1.1\ \text{mm}$ continuum survey image from the Bolocam Galactic Plane Survey (BGPS; Bally et al. 2010, bottom). Although YSOs and possible YSOs are found throughout the CMZ, about half of them are found in and around the Sgr B molecular complex ($l \sim +0.6\ \text{deg}$, $b \sim 0.0\ \text{deg}$).

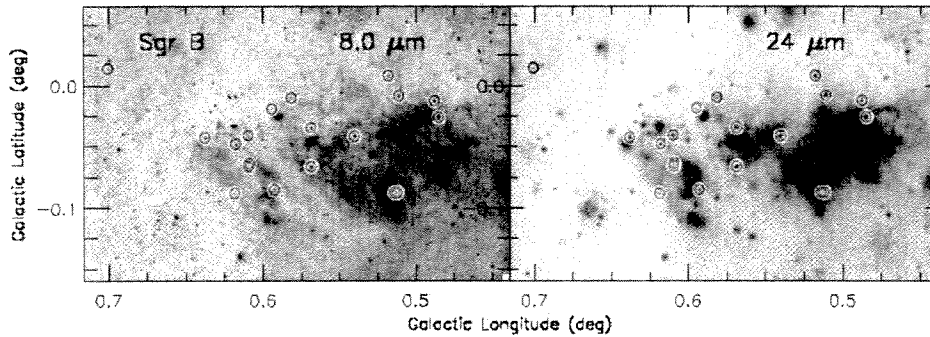


FIG. 18.— Same as in Figure 17, but in the Sgr B region. The YSOs and possible YSOs identified in our work are found on the edge of the strong $24\ \mu\text{m}$ emission regions.

TABLE 2
IRS SAMPLE OF CANDIDATE YSOS

Source ID SSTGC	R.A. (J2000.0)	Decl. (J2000.0)	Date of Observation	YSO Status			
				This work ^a	Felli et al.	Schuller et al.	Yusef-Zadeh et al.
531300	17 45 42.32	-28 52 47.3	May 2008	no
534806	17 45 43.57	-28 29 16.9	Oct. 2008	no	no
535007	17 45 43.64	-28 52 24.9	May 2008	no
536969	17 45 44.35	-29 01 13.8	Oct. 2008	no
540840	17 45 45.74	-28 48 29.7	May 2008	no
543691	17 45 46.76	-29 02 48.0	Oct. 2008	no
547817	17 45 48.24	-28 48 16.6	May 2008	no
550608	17 45 49.30	-28 50 58.8	Oct. 2008	no
563780	17 45 54.11	-28 58 12.1	Oct. 2008	maybe
564417	17 45 54.33	-29 00 03.2	Oct. 2008	no
579667	17 45 59.90	-28 53 07.2	Oct. 2008	no
580183	17 46 00.07	-29 01 49.3	Oct. 2008	no	yes
584613	17 46 01.67	-28 35 53.9	May 2008	no	no
588220	17 46 02.98	-28 52 45.0	Oct. 2008	no
600274	17 46 07.39	-28 45 32.0	May 2008	no
609613	17 46 10.71	-28 48 55.0	Oct. 2008	no
610642	17 46 11.08	-28 55 40.9	May 2008	maybe
612688	17 46 11.83	-28 47 12.0	May 2008	no
618018	17 46 13.81	-28 43 44.5	May 2008	maybe	yes
619522	17 46 14.33	-28 43 18.4	May 2008	maybe
619964	17 46 14.48	-28 36 39.7	May 2008	no	no	...	no
621858	17 46 15.18	-28 52 31.4	Oct. 2008	no
635358	17 46 20.01	-28 49 18.3	Oct. 2008	no
646021	17 46 23.89	-28 39 48.1	May 2008	no	no
648790	17 46 24.93	-28 47 18.2	Oct. 2008	no
653270	17 46 26.55	-28 18 59.9	Oct. 2008	maybe	yes	...	no
660708	17 46 29.27	-28 54 03.9	May 2008	no	no
670953	17 46 32.95	-28 42 16.3	May 2008	maybe	no
673151	17 46 33.76	-28 40 32.9	May 2008	no	no	...	no
679036	17 46 35.98	-28 43 58.2	May 2008	maybe	yes
689397	17 46 39.67	-28 41 27.8	May 2008	no	yes
696367	17 46 42.28	-28 33 26.3	May 2008	no	no	...	no
711462	17 46 47.82	-28 47 15.4	May 2008	no	yes	...	no
716531	17 46 49.64	-28 36 57.4	Oct. 2008	no	yes
718757	17 46 50.50	-28 43 33.4	May 2008	maybe	yes
719445	17 46 50.72	-28 31 24.7	May 2008	yes	yes	...	yes
721436	17 46 51.49	-28 33 06.2	May 2008	no	no
722141	17 46 51.68	-28 28 41.6	May 2008	yes	yes	...	yes
726327	17 46 53.29	-28 32 01.2	Oct. 2008	yes	yes
728480	17 46 54.13	-28 29 39.5	May 2008	yes	yes
732531	17 46 55.74	-28 32 20.2	Oct. 2008	no
738126	17 46 57.95	-28 35 54.5	May 2008	no
760679	17 47 07.45	-28 28 41.9	May 2008	yes
761771	17 47 07.94	-28 24 53.2	May 2008	yes
769305	17 47 11.27	-28 26 31.7	May 2008	yes
770393	17 47 11.75	-28 31 21.9	Oct. 2008	yes
771791	17 47 12.35	-28 31 10.8	Oct. 2008	no
772151	17 47 12.50	-28 24 15.6	May 2008	yes
772981	17 47 12.90	-28 32 05.5	Oct. 2008	yes
773985	17 47 13.34	-28 31 56.9	Oct. 2008	maybe
782872	17 47 17.31	-28 32 20.2	Oct. 2008	no	yes
786009	17 47 18.69	-28 27 31.7	May 2008	maybe
790317	17 47 20.55	-28 23 54.8	May 2008	maybe
797384	17 47 23.68	-28 23 34.6	May 2008	yes
799887	17 47 24.80	-28 15 56.8	May 2008	maybe	yes	...	no
801865	17 47 25.69	-28 24 40.2	May 2008	yes
803187	17 47 26.29	-28 22 01.5	May 2008	yes	yes ^b
803471	17 47 26.40	-28 24 43.7	May 2008	yes
806191	17 47 27.66	-28 26 28.4	Oct. 2008	maybe	no	...	yes
817031	17 47 32.97	-28 34 12.0	Oct. 2008	no	yes	...	no
817663	17 47 33.28	-28 24 47.4	May 2008	maybe

^a YSOs are marked as "yes", possible YSOs are marked as "maybe", and the remaining targets are marked as "no".

^b 4.5 μ m excess source without a 24 μ m counterpart.

TABLE 3
DATA REDUCTION SUMMARY FOR YSOs AND POSSIBLE YSOs

SSTGC ID	Baseline Module ^a	Flux Scaling Factor ^b					Excluded Data Set ^c
		SL1	SL2	SL3	LL1	LL2	
300758	LL2	1.25 ± 0.02	1.18 ± 0.06	1.15 ± 0.01	1.03 ± 0.03	...	
304239	SL1	...	0.89 ± 0.08	1.31 ± 0.02	1.80 ± 0.14	1.81 ± 0.14	SL2 (1st nod, N), LL (W)
360559	SL1	...	2.34 ± 0.06	2.70 ± 0.14	0.10 ± 0.01	0.10 ± 0.01	
370438	LL2	1.30 ± 0.10	1.17 ± 0.08	1.23 ± 0.03	0.98 ± 0.04	...	
372630	LL2	1.85 ± 0.07	1.60 ± 0.15	1.61 ± 0.02	0.96 ± 0.03	...	SL1 (E), SL2 (2nd nod, N, E)
496149	LL2	0.87 ± 0.03	0.85 ± 0.04	0.92 ± 0.01	1.00 ± 0.02	...	
524665	SL1	...	1.03 ± 0.06	1.06 ± 0.01	0.86 ± 0.01	0.82 ± 0.02	
563780	SL1	...	1.04 ± 0.05	1.06 ± 0.01	0.27 ± 0.01	0.25 ± 0.01	SL1 (W)
610642	LL2	0.97 ± 0.02	...	SL not available
618018	LL2	1.32 ± 0.02	1.34 ± 0.06	1.34 ± 0.01	1.02 ± 0.02	...	
619522	SL1	...	1.05 ± 0.03	1.03 ± 0.02	0.54 ± 0.02	0.58 ± 0.02	
653270	LL2	0.99 ± 0.01	0.99 ± 0.07	0.99 ± 0.01	1.02 ± 0.03	...	
670953	LL2	2.06 ± 0.11	2.09 ± 0.06	2.10 ± 0.02	1.00 ± 0.03	...	SL2 (1st nod)
679036	LL2	1.36 ± 0.10	1.33 ± 0.08	1.36 ± 0.01	0.94 ± 0.04	...	SL1 (W)
718757	LL2	1.66 ± 0.02	1.56 ± 0.09	1.57 ± 0.02	0.98 ± 0.02	...	SL2 (E)
719445	LL2	1.29 ± 0.04	1.25 ± 0.09	1.28 ± 0.01	0.97 ± 0.02	...	
722141	LL2	1.81 ± 0.11	1.77 ± 0.11	1.85 ± 0.02	0.96 ± 0.02	...	SL1 (W)
726327	LL2	1.81 ± 0.11	1.77 ± 0.11	1.85 ± 0.02	SL1 (W), SL2 (1st nod, N), LL1 (both nods)
728480	LL2	2.71 ± 0.04	2.60 ± 0.18	2.69 ± 0.02	1.01 ± 0.02	...	SL1 (W)
760679	LL2	1.53 ± 0.04	1.50 ± 0.05	1.51 ± 0.02	0.95 ± 0.01	...	SL1 (E)
761771	LL2	3.21 ± 0.50	2.93 ± 0.16	3.25 ± 0.13	0.98 ± 0.02	...	
769305	LL2	1.42 ± 0.06	1.39 ± 0.09	1.42 ± 0.02	1.00 ± 0.04	...	
770393	LL2	3.29 ± 0.04	3.12 ± 0.18	3.28 ± 0.02	LL1 (both nods)
772151	LL2	1.37 ± 0.08	1.35 ± 0.05	1.54 ± 0.03	1.01 ± 0.06	...	SL1 (S), SL2 (W)
772981	LL2	2.20 ± 0.08	1.88 ± 0.01	1.99 ± 0.01	0.64 ± 0.02	...	SL2 (1st nod, N), LL1 (N)
773985	LL2	7.87 ± 1.59	6.02 ± 0.10	6.51 ± 0.14	0.90 ± 0.03	...	LL1 (N, S)
786009	LL2	1.45 ± 0.03	1.81 ± 0.13	1.89 ± 0.06	1.00 ± 0.02	...	SL1 (1st nod, S)
790317	LL2	1.45 ± 0.05	1.45 ± 0.09	1.49 ± 0.01	0.93 ± 0.02	...	SH (S)
797384	LL2	1.33 ± 0.05	1.34 ± 0.09	1.39 ± 0.01	0.99 ± 0.03	...	
799887	LL2	1.02 ± 0.06	1.02 ± 0.07	1.00 ± 0.01	0.96 ± 0.02	...	
801865	SL1	...	0.93 ± 0.07	1.00 ± 0.01	0.05 ± 0.01	0.04 ± 0.01	
803187	LL2	1.33 ± 0.13	1.31 ± 0.08	1.33 ± 0.01	0.98 ± 0.03	...	
803471	LL2	1.83 ± 0.04	1.85 ± 0.13	1.90 ± 0.01	1.03 ± 0.03	...	
806191	LL2	1.37 ± 0.14	1.10 ± 0.03	...	N from all sky positions, SL2 (W), SL3 (both nods, S)
817663	SL1	...	0.69 ± 0.04	0.72 ± 0.05	0.42 ± 0.01	0.48 ± 0.01	SL2 (E)

NOTE. — IRS modules: short-high (SH; 9.9 μm –19.6 μm , $\lambda/\Delta\lambda \sim 600$), long-high (LH; 18.7 μm –37.2 μm , $\lambda/\Delta\lambda \sim 600$), short-low (SL [1st order SL1 7.4 μm –14.5 μm , 2nd order SL2 5.2 μm –7.7 μm , 3rd order SL3 7.3 μm –8.7 μm , $\lambda/\Delta\lambda \sim 60$ –127]), and long-low (LL [1st order LL1 19.5 μm –38.0 μm , 2nd order LL2 14.0 μm –21.3 μm , 3rd order LL3 19.4 μm –21.7 μm , $\lambda/\Delta\lambda \sim 57$ –126]).

^a IRS module selected as a baseline for the flux calibration. See text.

^b Adopted scaling factor in each module. The value represents the scaled flux divided by the original flux.

^c Specific modules/orders that contain defective data. These were excluded in the spectral analysis. “NSEW” denote background observations northern/southern/eastern/western from the source target. “Nod” represents a specific nod position for a set of target spectra.

TABLE 4
CO₂ ICE DECOMPOSITION FOR YSOs AND POSSIBLE YSOs

SSTGC ID	$\log N_{\text{col}}(\text{polar})$ (cm ⁻²)	$\log N_{\text{col}}(\text{apolar})$ (cm ⁻²)	$\log N_{\text{col}}(\text{shoulder})$ (cm ⁻²)	$\log N_{\text{col}}(\text{diluted})$ (cm ⁻²)	$\log N_{\text{col}}(\text{pure})$ (cm ⁻²)	$\log N_{\text{col}}(\text{total})$ (cm ⁻²)	χ^2_{tot}	N_{tot}	YSO Status
300758	17.08 ± 0.08	17.11 ± 0.06	16.88 ± 0.06	< 16.17	< 16.78	17.57 ± 0.03	488	152	maybe
304239	18.31 ± 0.08	17.98 ± 0.06	17.40 ± 0.16	< 16.17	17.29 ± 0.25	18.54 ± 0.04	1615	152	yes
360559	17.40 ± 0.17	17.41 ± 0.15	16.88 ± 0.21	16.54 ± 0.31	< 16.78	17.79 ± 0.01	2181	152	maybe
370438	17.83 ± 0.19	17.42 ± 0.05	17.16 ± 0.08	< 16.17	< 16.78	18.06 ± 0.12	280	152	maybe
372630	17.06 ± 0.16	17.48 ± 0.01	17.11 ± 0.05	< 16.17	< 16.78	17.73 ± 0.06	237	152	maybe
496149	17.70 ± 0.10	17.42 ± 0.04	16.97 ± 0.11	< 16.17	< 16.78	17.95 ± 0.04	99	152	maybe
524665	17.75 ± 0.01	17.41 ± 0.05	17.16 ± 0.02	< 16.17	16.94 ± 0.06	18.02 ± 0.01	424	152	yes
563780	17.06 ± 0.01	17.05 ± 0.07	16.75 ± 0.06	< 16.17	< 16.78	17.39 ± 0.11	594	152	maybe
610642	17.31 ± 0.06	16.80 ± 0.09	16.79 ± 0.04	< 16.17	< 16.78	17.54 ± 0.03	219	118	maybe
618018	17.18 ± 0.03	17.10 ± 0.03	16.86 ± 0.03	< 16.17	< 16.78	17.55 ± 0.02	535	152	maybe
619522	17.60 ± 0.69	17.19 ± 0.30	17.07 ± 0.23	< 16.17	< 16.78	17.83 ± 0.62	1027	152	maybe
653270	17.99 ± 0.05	16.79 ± 0.21	16.89 ± 0.11	16.82 ± 0.23	17.39 ± 0.17	18.14 ± 0.04	980	152	maybe
670953	17.54 ± 0.39	16.90 ± 0.30	16.78 ± 0.20	16.64 ± 0.31	< 16.78	17.75 ± 0.14	710	152	maybe
679036	17.26 ± 0.15	17.17 ± 0.04	16.90 ± 0.06	< 16.17	< 16.78	17.62 ± 0.04	473	152	maybe
718757	17.76 ± 0.03	17.59 ± 0.01	16.96 ± 0.01	16.52 ± 0.04	< 16.78	18.04 ± 0.02	658	152	maybe
719445	17.88 ± 0.03	17.32 ± 0.04	17.14 ± 0.03	16.36 ± 0.15	< 16.78	18.07 ± 0.03	889	152	yes
722141	17.80 ± 0.02	17.48 ± 0.01	17.12 ± 0.02	16.24 ± 0.12	< 16.78	18.03 ± 0.01	990	152	yes
726327	17.47 ± 0.10	17.30 ± 0.07	17.08 ± 0.07	< 16.17	< 16.78	17.80 ± 0.01	867	152	yes
728480	17.83 ± 0.01	17.32 ± 0.01	17.04 ± 0.01	16.20 ± 0.03	< 16.78	18.00 ± 0.01	1175	152	yes
760679	17.70 ± 0.01	17.34 ± 0.02	17.11 ± 0.03	16.23 ± 0.06	< 16.78	17.94 ± 0.01	834	152	yes
761771	18.24 ± 0.03	17.73 ± 0.01	17.33 ± 0.02	16.42 ± 0.05	< 16.78	18.40 ± 0.02	963	152	yes
769305	18.21 ± 0.12	18.03 ± 0.06	17.57 ± 0.05	16.68 ± 0.04	< 16.78	18.49 ± 0.04	2347	152	yes
770393	17.48 ± 0.03	17.23 ± 0.01	16.78 ± 0.01	< 16.17	< 16.78	17.74 ± 0.02	1077	152	yes
772151	18.13 ± 0.10	17.84 ± 0.06	17.41 ± 0.07	16.56 ± 0.31	< 16.78	18.37 ± 0.05	1081	152	yes
772981	17.15 ± 0.15	17.19 ± 0.07	16.95 ± 0.05	< 16.17	< 16.78	17.60 ± 0.13	630	152	yes
773985	17.26 ± 0.14	17.24 ± 0.03	16.85 ± 0.05	< 16.17	< 16.78	17.64 ± 0.04	340	152	maybe
786009	17.43 ± 0.02	17.16 ± 0.02	16.81 ± 0.02	< 16.17	< 16.78	17.70 ± 0.01	465	152	maybe
790317	17.59 ± 0.19	17.37 ± 0.02	16.94 ± 0.11	< 16.17	< 16.78	17.86 ± 0.10	573	152	maybe
797384	17.88 ± 0.02	17.47 ± 0.03	17.21 ± 0.01	16.23 ± 0.08	< 16.78	18.09 ± 0.01	1109	152	yes
799887	17.60 ± 0.18	17.87 ± 0.10	17.50 ± 0.06	16.77 ± 0.32	17.27 ± 0.42	18.23 ± 0.03	817	152	maybe
801865	17.88 ± 0.01	17.66 ± 0.06	17.32 ± 0.02	16.38 ± 0.10	< 16.78	18.16 ± 0.03	698	152	yes
803187	18.17 ± 0.03	17.56 ± 0.05	17.28 ± 0.04	< 16.17	< 16.78	18.31 ± 0.01	1648	152	yes
803471	17.84 ± 0.02	17.58 ± 0.03	17.24 ± 0.03	16.41 ± 0.04	< 16.78	18.11 ± 0.01	1253	152	yes
806191	17.92 ± 0.04	17.24 ± 0.07	17.12 ± 0.05	16.60 ± 0.13	< 16.78	18.08 ± 0.02	657	152	maybe
817663	17.06 ± 0.14	17.28 ± 0.13	16.98 ± 0.21	< 16.17	< 16.78	17.54 ± 0.08	789	152	maybe
Known Stars									
425399	17.26 ± 0.21	< 16.79	< 16.65	< 16.17	< 16.78	17.38 ± 3.38	330	152	known stars
564417	17.68 ± 0.63	17.00 ± 0.29	17.01 ± 0.40	16.37 ± 0.21	< 16.78	17.86 ± 3.86	1205	152	known stars
619964	17.37 ± 0.32	16.80 ± 0.02	16.80 ± 0.17	< 16.17	< 16.78	17.58 ± 3.58	1076	152	known stars
660708	17.18 ± 0.40	17.55 ± 0.88	17.23 ± 0.68	< 16.17	17.41 ± 0.63	17.97 ± 3.97	1856	151	known stars
696367	17.72 ± 0.66	17.21 ± 0.43	16.91 ± 0.27	16.35 ± 0.18	< 16.78	17.90 ± 3.90	499	152	known stars

TABLE 5
GAS-PHASE ABSORPTION FEATURES OF YSOs AND POSSIBLE YSOs

SSTGC ID	C ₂ H ₂			HCN			CO ₂			CO ₂ gas to solid ratio
	T_{ex} (K)	$\log N_{\text{col}}$ (cm ⁻²)	Abundance ^a	T_{ex} (K)	$\log N_{\text{col}}$ (cm ⁻²)	Abundance ^a	T_{ex} (K)	$\log N_{\text{col}}$ (cm ⁻²)	Abundance ^a	
524665	400 ± 190	16.9 ± 0.1	-5.4 ± 0.1	400 ± 70	17.0 ± 0.2	-5.3 ± 0.2	200 ± 100	17.2 ± 0.3	-5.1 ± 0.3	0.15 ± 0.10
726327	100 ± 50	16.4 ± 0.3	-6.3 ± 0.3	0.04 ± 0.03
728480	300 ± 170	15.7 ± 0.3	-6.9 ± 0.3	200 ± 170	16.2 ± 0.2	-6.4 ± 0.2	0.02 ± 0.01
761771	100 ± 50	16.7 ± 0.3	-6.1 ± 0.3	0.02 ± 0.01
772151	100 ± 173	16.6 ± 0.3	-6.2 ± 0.3	0.02 ± 0.01
797384	100 ± 160	16.0 ± 0.2	-6.7 ± 0.2	100 ± 50	16.6 ± 0.1	-6.1 ± 0.1	0.03 ± 0.01
801865	400 ± 500	16.5 ± 0.4	-6.3 ± 0.4	100 ± 158	16.9 ± 0.2	-5.9 ± 0.2	0.05 ± 0.03
803187	300 ± 170	16.4 ± 0.2	-6.4 ± 0.2	100 ± 580 ^b	16.4 ± 0.6 ^b	-6.4 ± 0.6	100 ± 50	16.8 ± 0.2	-6.0 ± 0.2	0.03 ± 0.01
803471	200 ± 160	16.0 ± 0.2	-6.6 ± 0.2	100 ± 150	16.7 ± 0.2	-5.9 ± 0.2	0.04 ± 0.02

^a Abundance relative to molecular hydrogen, $\log N/N(\text{H}_2)$.

^b Two local χ^2 minima were found at $T_{\text{ex}} = 100 \text{ K}$, $\log N_{\text{col}} = 16.4$ and $T_{\text{ex}} \approx 700 \text{ K}$, $\log N_{\text{col}} \approx 16.7$.

TABLE 6
 A_V FOR GC YSOs AND POSSIBLE YSOs

SSTGC ID	A_V (SL+LL) (mag)	A_V (SH+LH) (mag)	A_V (foreground) ^a (mag)
300758	33.3 ± 11.4	33.7 ± 23.6	40 ± 3
304239	28.7 ± 7.0	27.7 ± 4.5	43 ± 4
360559	50.4 ± 15.2	48.5 ± 9.9	46 ± 9
370438	53.3 ± 6.8	30.8 ± 44.1	62 ± 17
372630	49.6 ± 9.5	36.0 ± 4.1	62 ± 17
496149	38.8 ± 7.4	19.9 ± 7.5	31 ± 12
524665	20.5 ± 10.7	40.4 ± 12.2	43 ± 9
563780	60.0 ± 9.9	39.7 ± 3.3	48 ± 8
610642	...	24.6 ± 9.5	28 ± 2
618018	34.3 ± 9.6	27.0 ± 2.4	27 ± 5
619522	34.1 ± 6.4	48.5 ± 3.3	27 ± 2
653270	17.6 ± 0.4	22.3 ± 0.8	22 ± 3
670953	44.7 ± 1.5	38.8 ± 1.6	31 ± 8
679036	51.3 ± 3.8	43.3 ± 4.1	46 ± 12
718757	31.9 ± 8.4	31.8 ± 0.3	76 ± 22
719445	44.9 ± 1.7	53.5 ± 2.1	30 ± 4
722141	39.5 ± 1.9	36.7 ± 1.6	19 ± 5
726327	48.0 ± 5.2	43.3 ± 2.1	30 ± 4
728480	44.3 ± 4.0	39.8 ± 0.3	39 ± 11
760679	48.8 ± 4.4	48.9 ± 0.8	29 ± 2
761771	69.5 ± 7.3	61.1 ± 1.9	47 ± 8
769305	76.5 ± 5.3	53.5 ± 2.3	47 ± 14
770393	30.4 ± 1.0	29.9 ± 0.5	36 ± 5
772151	60.2 ± 20.7	64.5 ± 6.7	24 ± 3
772981	48.3 ± 9.8	40.7 ± 0.7	36 ± 2
773985	70.6 ± 6.9	42.4 ± 4.2	36 ± 2
786009	40.9 ± 7.4	34.2 ± 0.4	37 ± 10
790317	45.4 ± 14.9	47.5 ± 1.6	31 ± 4
797384	55.0 ± 5.7	55.1 ± 0.9	31 ± 1
799887	36.2 ± 1.5	36.2 ± 2.3	35 ± 1
801865	66.7 ± 9.4	57.0 ± 7.0	31 ± 4
803187	61.3 ± 1.7	57.6 ± 1.4	27 ± 1
803471	46.8 ± 2.1	52.1 ± 0.8	31 ± 4
806191	55.4 ± 19.8	55.7 ± 0.9	24 ± 3
817663	32.6 ± 14.0	30.7 ± 2.0	29 ± 1

^a Based on the 2MASS and IRAC color-magnitude diagrams of GC red giant branch stars within $2'$ of the source (Schultheis et al. 2009).

TABLE 7
PHOTOMETRIC PROPERTIES OF YSOs AND POSSIBLE YSOs

SSTGC ID	UKIDSS ^a			IRAC ^b				Synthetic [24] ^c (mag)	SCUBA ^d	
	<i>J</i> (mag)	<i>H</i> (mag)	<i>K</i> (mag)	[3.6] (mag)	[4.5] (mag)	[5.8] (mag)	[8.0] (mag)		450 μ m (Jy)	850 μ m (Jy)
300758	19.06 ± 0.11	14.77 ± 0.01	12.36 ± 0.01	10.2	9.0	7.8	6.2	0.7	12.2 ± 1.4	0.3 ± 0.1
304239	16.88 ± 0.18	12.8	10.2	8.6	7.7	2.2	< 5.0	0.2 ± 0.1
360559	...	18.74 ± 0.29	14.60 ± 0.03	12.2	11.1	9.3	7.6	1.7
370438	14.93 ± 0.04	11.9	10.0	8.9	7.4	1.8
372630	...	16.39 ± 0.03	13.63 ± 0.01	10.3	8.8	7.7	6.5	1.5	1.9 ± 0.8	0.1 ± 0.1
496149	...	16.93 ± 0.11	13.89 ± 0.03	12.0	11.0	9.6	8.2	1.3
524665	15.71 ± 0.10	11.4	8.6	7.1	6.1	0.5	428.5 ± 1.1	36.9 ± 0.1
563780	18.56 ± 0.10	15.93 ± 0.04	14.09 ± 0.04	11.6	10.8	8.2	...	0.7
610642	18.97 ± 0.15	...	12.56 ± 0.01	9.8	8.0	6.6	4.8	-0.2
618018	15.33 ± 0.01	14.52 ± 0.01	13.79 ± 0.02	...	9.6	7.9	6.5	0.5
619522	...	14.50 ± 0.01	11.97 ± 0.01	10.4	9.3	8.4	7.7	2.0
653270	...	16.43 ± 0.06	10.98 ± 0.01	8.3	7.1	6.1	5.7	2.3	26.2 ± 1.6	1.1 ± 0.1
670953	...	17.38 ± 0.15	14.92 ± 0.06	11.4	8.9	7.1	6.1	0.6
679036	17.05 ± 0.02	16.50 ± 0.04	14.66 ± 0.04	11.3	9.4	7.6	6.1	0.7	8.1 ± 0.7	1.3 ± 0.1
718757	15.41 ± 0.07	10.9	9.3	7.8	6.0	-0.3
719445	...	16.50 ± 0.04	13.51 ± 0.01	11.4	9.1	7.7	6.0	1.3
722141	15.35 ± 0.05	13.0	10.9	9.3	7.3	0.3
726327	18.29 ± 0.07	13.55 ± 0.01	11.55 ± 0.01	9.3	7.9	6.6	4.9
728480	13.20 ± 0.01	11.3	10.3	9.3	7.5	-0.3	47.9 ± 0.9	8.0 ± 0.1
760679	15.67 ± 0.07	...	10.3	8.3	6.5	-0.2	21.0 ± 0.9	0.9 ± 0.1
761771	15.43 ± 0.06	13.2	10.6	...	8.0	1.3
769305	18.50 ± 0.08	18.23 ± 0.19	...	11.8	8.8	7.2	5.3	-0.5	492.6 ± 1.2	28.1 ± 0.1
770393	...	17.17 ± 0.07	13.81 ± 0.01	10.4	8.7	7.2	5.1
772151	15.88 ± 0.01	14.85 ± 0.01	14.22 ± 0.02	13.1	11.7	10.2	...	2.1	568.3 ± 1.4	21.5 ± 0.1
772981	...	16.11 ± 0.03	13.54 ± 0.01	11.2	9.8	8.2	7.0	0.0
773985	14.30 ± 0.02	12.0	10.7	-0.7
786009	10.7	-0.6	62.4 ± 1.0	2.0 ± 0.1
790317	...	17.21 ± 0.07	14.40 ± 0.02	...	10.8	9.2	7.5	0.5	7214.4 ± 3.5	326.2 ± 0.3
797384	18.52 ± 0.08	15.59 ± 0.02	13.72 ± 0.01	...	9.4	7.7	5.6	-0.2	340.4 ± 3.6	4.4 ± 0.4
799887	14.24 ± 0.02	9.4	7.2	5.8	5.3	2.7
801865	...	17.07 ± 0.07	11.3	10.3	8.8	3.3
803187	17.39 ± 0.03	16.61 ± 0.05	14.39 ± 0.02	12.2	9.0	7.2	5.1	-1.1
803471	13.50 ± 0.01	10.5	8.8	7.5	6.0	-0.1
806191	16.52 ± 0.01	15.43 ± 0.01	14.61 ± 0.03	12.6	11.0	9.1	7.4	1.6	243.5 ± 1.2	11.3 ± 0.1
817663	...	16.35 ± 0.03	14.34 ± 0.02	12.6	11.5	10.1	8.9	2.3	133.9 ± 1.1	8.1 ± 0.1

^a Aperture3 magnitudes from UKIDSS DR2 (Warren et al. 2007).

^b Systematic errors of IRAC photometry were determined to be 0.1 mag, 0.1 mag, 0.15 mag, and 0.2 mags for channels 1, 2, 3, and 4, respectively, by comparing the Ramírez et al. (2008) values with the measurements from the GLIMPSE II catalog (Churchwell et al. 2009).

^c Synthetic photometry based on IRS spectra.

^d Fluxes from SCUBA Legacy Catalogues (Di Francesco et al. 2008).

TABLE 8
SED FITTING RESULTS AND MASS ESTIMATES FROM RADIO CONTINUUM

SSTGC ID	$\log M_*$ (M_\odot)	$\log L_{tot}$ (L_\odot)	A_V (ISM) (mag)	$\log M_{env}$ ($M_\odot \text{ yr}^{-1}$)	$\log \text{Age}$ (yr)	Radio Modeling	
						$\log M_*$ (M_\odot)	References
300758	1.03 ± 0.05	3.64 ± 0.23	22.3 ± 2.9	-3.38 ± 0.55	4.43 ± 0.47	1.18	1
304239	0.88 ± 0.08	3.18 ± 0.28	31.2 ± 7.1	-3.66 ± 0.37	4.44 ± 0.81		
360559	1.01	3.37	30.7 ± 4.1	-3.39	4.12		
370438	0.91 ± 0.06	3.22 ± 0.27	25.1 ± 4.4	-3.69 ± 0.34	3.89 ± 0.78		
372630	0.97 ± 0.09	3.34 ± 0.24	24.1 ± 3.4	-3.57 ± 0.24	3.29 ± 0.22		
496149	0.97 ± 0.05	3.51 ± 0.19	24.0 ± 5.0	-3.73 ± 0.37	4.72 ± 0.75		
524665	1.04 ± 0.05	3.90 ± 0.16	33.9 ± 6.1	-3.07 ± 0.27	4.94 ± 0.31		
563780	0.99	3.45	20.0 ± 9.0	...	4.53		
610642	1.06 ± 0.09	3.84 ± 0.29	23.6 ± 2.5	-4.01 ± 0.71	4.95 ± 0.96		
618018	0.97 ± 0.02	3.35 ± 0.10	20.0	-3.49 ± 0.63	4.53 ± 0.20		
619522	0.98	3.40	20.0	-3.68	4.58		
653270	1.17 ± 0.09	4.32 ± 0.24	39.3 ± 1.2	...	6.17 ± 0.09		
670953	1.37 ± 0.14	4.32 ± 0.31	33.8 ± 7.7	-2.72 ± 0.27	3.26 ± 0.39		
679036	0.98 ± 0.01	3.39 ± 0.08	20.0	-3.74 ± 0.55	4.57 ± 0.06		
718757	1.13 ± 0.07	3.92 ± 0.13	33.1 ± 5.8	-3.52 ± 0.45	4.14 ± 0.52		
719445	0.88 ± 0.07	2.94 ± 0.16	22.0 ± 2.3	-4.19 ± 0.18	3.57 ± 0.37		
722141	1.04 ± 0.05	3.95 ± 0.15	35.8 ± 5.0	-3.22 ± 0.27	5.07 ± 0.26		
726327	1.36 ± 0.05	4.67 ± 0.31	20.6 ± 1.1	-2.85 ± 0.45	4.32 ± 0.69	1.27	2
728480	1.18 ± 0.05	3.91 ± 0.11	22.7 ± 3.8	-3.47 ± 0.20	3.72 ± 0.46	1.26	3
760679	1.42	4.97	40.0	...	5.00	1.26	4
761771	1.00	3.96	20.0	...	4.89		
769305	1.24 ± 0.01	4.29 ± 0.04	20.0	-3.04 ± 0.09	3.83 ± 0.10	1.27	5
770393	1.25 ± 0.06	4.53 ± 0.14	35.9 ± 2.8	-4.08 ± 0.11	4.56 ± 0.42		
772151	1.14	3.91	20.0	...	3.91	1.26	6
772981	1.20 ± 0.03	3.84 ± 0.13	20.0 ± 0.1	-3.39 ± 0.18	3.48 ± 0.19		
773985	1.21 ± 0.09	4.24 ± 0.26	21.8 ± 1.9	-3.17 ± 0.27	4.04 ± 0.48		
786009	1.15 ± 0.06	4.12 ± 0.14	33.9 ± 6.9	-3.58 ± 0.36	4.51 ± 0.57		
790317	1.13 ± 0.07	3.74 ± 0.18	21.7 ± 2.0	-3.40 ± 0.25	3.65 ± 0.53		
797384	1.20 ± 0.04	4.05 ± 0.24	20.0	-3.07 ± 0.34	3.92 ± 0.58	1.29	7
799887	1.11 ± 0.04	3.67 ± 0.08	20.0	-2.24 ± 0.09	3.19 ± 0.06		
801865	0.93 ± 0.02	3.15 ± 0.18	20.0	-2.96 ± 0.26	4.70 ± 0.09		
803187	1.22	4.26	20.0 ± 9.0	...	3.80	1.39	8
803471	1.22 ± 0.06	3.93 ± 0.16	20.2 ± 0.4	-3.27 ± 0.22	3.49 ± 0.48		
806191	1.05	3.61	20.0 ± 9.0	...	4.17		
817663	0.92 ± 0.04	3.01 ± 0.21	21.8 ± 3.8	-3.54 ± 0.63	4.34 ± 0.36		

REFERENCES. — References for radio observations: (1) Yusef-Zadeh et al. (2009); (2) GPSR5 0.488-0.028, Mehringer et al. (1992); Becker et al. (1994); (3) #8, Mehringer et al. (1992); Mehringer (1995); (4) 2LC 000.563-0.044, Mehringer et al. (1992); Yusef-Zadeh et al. (2004); Lazio & Cordes (2008); (5) GPSR5 0.602-0.037, Becker et al. (1994); Lazio & Cordes (1998); Yusef-Zadeh et al. (2004); Lazio & Cordes (2008); (6) 1LC 000.635-0.020, Lazio & Cordes (1998); White et al. (2005); (7) SGR B2 HII P, Mehringer et al. (1993); Yusef-Zadeh et al. (2004); (8) GPSR5 0.693-0.046, Zoonematkermani et al. (1990); Becker et al. (1994); Lazio & Cordes (1998); Yusef-Zadeh et al. (2004); White et al. (2005); Lazio & Cordes (2008).

